<u>Title:</u> Annexin and calcium-regulated priming of legume root cells for endosymbiotic infection

Authors:

Ambre Guillory[1§], Joëlle Fournier[1§], Audrey Kelner[1§], Karen Hobecker[2], Marie-Christine Auriac[1], Lisa Frances[1], Anaïs Delers[1], Aurélie Le Ru[3], Jean Keller[4], Pierre-Marc Delaux[4], Caroline Gutjahr[2], Nicolas Frei Dit Frey[4] and Fernanda de Carvalho-Niebel[1*]

Affiliations :

[1]LIPME, INRAE, CNRS, Université de Toulouse, Castanet-Tolosan, France.

[2]Max-Planck-Institute of Molecular Plant Physiology, Potsdam-Golm, Germany.

[3]FRAIB-TRI imaging platform, Université de Toulouse, CNRS, UPS, Castanet-Tolosan, France.

[4]LRSV, Université de Toulouse, CNRS, UPS, Toulouse INP, Castanet-Tolosan, France.

[§]these authors contributed equally to this work

[*]Correspondence to: Fernanda de Carvalho-Niebel (fernanda.de-carvalho-niebel@inrae.fr)

Abstract

Legumes establish endosymbioses with arbuscular mycorrhizal (AM) fungi or rhizobia bacteria to improve mineral nutrition. Symbionts are then hosted in privileged habitats, root cortex (for AM fungi) or nodules (for rhizobia), for efficient nutrient exchanges. To reach them, the plant creates trans-vacuolar cytoplasmic bridges, key for predicting and directing AM fungi hyphae or rhizobia-filled infection threads (ITs) entry. Yet, mechanisms underlying this pre-infection cellular remodelling are poorly studied. Here we show that unique ultrastructural changes and Ca^{2+} spiking signals closely linked to MtAnn1 annexin cellular dynamics, shape rhizobia-primed cells. Loss of *MtAnn1* function in *M. truncatula* affects peak amplitude, cytoplasm configuration and rhizobia infection, consistent with MtAnn1's role in regulating this priming state. *MtAnn1,* mainly recruited during evolution in plants establishing endosymbioses, also appears involved in the ancient AM symbiosis in *M. truncatula*. Together, our work suggests MtAnn1 as part of an ancient Ca^{2+}-regulatory module for transcellular endosymbiotic root infection.

Introduction

Plants benefit from associations with microbes in the soil which improve the acquisition of essential nutrients for growth. These associations include the ancestral symbiosis with arbuscular mycorrhizal (AM) fungi providing phosphorous supply, or the more recently evolved interactions with endosymbiotic bacteria for nitrogen acquisition[1,2]. Microbial endosymbionts are hosted in privileged intracellular niches, where optimal conditions are met for efficient nutrient exchange (e.g. the root cortex hosting arbuscules formed by AM fungi, or root nodules, hosting nitrogen-fixing bacteria). Extensive studies on model legumes such as *Medicago truncatula*, combined with evolution-based studies across broad species range revealed that nodule-forming nitrogen-fixing endosymbiosis (RNS) evolved ~100 million years ago in species from related angiosperm plant lineages, by co-opting signalling components from the ancient AM symbiosis and recruiting new key genes through neo-functionalization and/or rewiring of expression[2-4]. Remarkably, AM and RN symbioses share a common symbiotic pathway that uses calcium (Ca^{2+}) as a key secondary messenger to trigger downstream signalling[5,6]. Indeed, the perception of mycorrhizal Myc and rhizobial Nod factor signals induces Ca^{2+} oscillations (spiking) in and around the root hair nucleus through the concerted action of nuclear envelope channel/pump complexes[5-7]. While Ca^{2+} spiking is critical in the nucleus (after its decoding by Ca^{2+}/calmodulin-dependent protein kinases CCaMK or Does not Make Infection, DMI3)[8,9] to regulate host transcriptional reprogramming[10-12], the functional relevance of sustained Ca^{2+}spiking in the cytoplasmic compartment has not yet been established. The rhizobia- and AM-induced *MtAnn1*[13] and *MtAnn2*[14] genes, which encode Ca^{2+}-binding and phospholipid membrane-associated proteins of the annexin family, whose members are involved in the regulation of ionic conductance and cytoplasmic Ca^{2+} signals[15-19], are potential players in this process.

Following signal exchanges to reach compatibility, infection of root tissues by AM fungi or rhizobia bacteria occurs in most legumes transcellularly, through the *de novo* construction of apoplastic compartments, delimited by host cell wall/ membrane interfaces, which physically separate microsymbionts from the host cytoplasm[20,21]. The hyphae of AM fungi progress through epidermal and cortical root tissues until the fungus reaches the inner cortex to form

65 highly branched arbuscules inside plant cells. Arbuscules comprise a massive network of
66 membrane tubules at the symbiotic host-fungus interface[22,23], which likely ensures the release
67 of nutrients, particularly phosphate, to the plant. In RNS, rhizobia enter the roots of most
68 legume species, *via* apoplastic tubular structures called infection threads (ITs)[21]. ITs are
69 formed in root hairs after rhizobia have been entrapped and enclosed in a globular infection
70 chamber, a process orchestrated by dynamic changes in the cytoskeleton-plasma-membrane-
71 cell wall interface[24-26]. ITs grow polarly from cell to cell towards the developing nodule forming
72 underneath[27,28], and these two programs must be tightly synchronized before a fully
73 functional nodule is formed under the influence of key plant hormones, intercellular signalling
74 and long-distance regulatory pathways[29-32].

75 There are striking similarities in the cellular events that underlie early penetration by AM
76 fungal hyphae and rhizobia-containing ITs. In both cases, plant root cells undergo a radical
77 reprogramming that results in the formation of characteristic cytoplasmic columns, known as
78 Pre-Penetration Apparatus (PPA)[33] or Pre-Infection Thread (PIT)[34] to guide the transcellular
79 passage of AM fungal hyphae and rhizobia-filled ITs, respectively. Remarkably, such
80 endosymbiosis-related cytoplasmic remodelling is not seen in pathogen interactions[35]. Thus,
81 a conserved and probably ancient cellular mechanism is used to commit plant cells to
82 beneficial endosymbioses. In this process, differentiated root cells with a large central vacuole
83 switch to an activated symbiotic state (hereafter referred to as pre-infection priming), with
84 characteristic trans-vacuolar cytoplasmic strands radiating from the nucleus before a
85 cytoplasmic bridge is actually formed. Parallels have been drawn between PIT/PPA and
86 phragmosome formation in mitotically dividing cells, as similarities have been demonstrated
87 on the tight control of the plant cell division status, membrane trafficking and microtubule
88 dynamics during fungal and/or rhizobial infection[36-40]. The development of fluorescent protein
89 fusions labelling the cytoplasm or endoplasmic reticulum network (ER) has made it possible
90 to visualize the dynamics of cytoplasmic reprogramming *in vivo* during PPA and PIT
91 formation[33,41]. These studies showed that this remodelling, guided by the nucleus, occurs in
92 root hairs to accompany IT progression and in neighbouring cortical cells to anticipate IT
93 passage. Primed cortical cells show a low-frequency Ca^{2+} spiking signature that switches to a
94 high frequency at the onset of infection by AM fungi or rhizobia[42]. CCaMK is critical for
95 endosymbiotic infection and can trigger cytoplasmic remodelling in the cortex in the absence
96 of symbionts[43]. Thus, CCaMK-mediated signalling can bypass early symbiotic activation to
97 trigger the priming response, at least in the cortex. These results imply that symbiotic
98 commitment of plant cells involves fine-tuned regulation of Ca^{2+} spiking signatures, yet the
99 underlying genetic pathways or molecular players have not been identified.

100 In this study, using resolutive microscopy methods in different *M. truncatula* genetic
101 backgrounds, we provide novel insights on ultrastructural rearrangements and *in vivo* Ca^{2+}
102 signalling dynamics in plant cells preparing for rhizobia infection. We demonstrate that this
103 cellular reprogramming is marked by an intimate link between Ca^{2+} spiking and the annexin
104 MtAnn1. MtAnn1 is key for shaping cytoplasmic reprograming for infection, *via* a genetic
105 pathway controlled by the master symbiotic transcription factor Nodule Inception (NIN)[3].
106 Through phylogenetics and mutant phenotyping, we provide evidence that *MtAnn1*, recruited
107 during evolution in plants establishing root endosymbioses, likely plays an ancestral role for
108 successful rhizobia and AM fungi infection. We propose that *MtAnn1* was recruited to shape
109 calcium-regulated transvacuolar cytoplasmic rearrangements for successful endosymbiotic
110 root infection.

111 ## Results

112 ### Cell-specific ultrastructural changes in plant cells prior to IT entry

113 Previous light microscopy studies reported PIT cellular rearrangements in vetch or
114 *Medicago* nodule or root cells[34,40]. Here, we set up an adapted methodology to gain access to
115 ultrastructural changes underlying rhizobia pre-infection priming in *M. truncatula*. Segments
116 of early infected roots, harvested 5-6 dpi with rhizobia, were prepared for light and
117 transmission electron microscopy (TEM) using an Epon-embedding procedure. These analyses
118 revealed specific cytoplasmic rearrangements in primed outer cortical cells (C1) next to an
119 infected root hair site (Fig 1A-C). TEM analyses showed that the thick cytoplasmic bridge is
120 highly enriched in endoplasmic reticulum (ER) (white arrows, Fig. 1E) and large quantities of
121 small vacuole-like structures with sizes ranging from 0,5 to 5 µm (v in Fig. 1E). These activated
122 cells also feature an unusually high density of mitochondria, often elongated, around the
123 nucleus (m in Fig. 1E). This pre-infection priming structural configuration was never observed
124 in other cells of the primordia, even in actively dividing meristematic cells of the C3 cell layer
125 (Fig. 1C-D). At a later stage, when the IT has progressed across this small vacuole- and ER-rich
126 cytoplasmic bridge, the nucleus is often found in close proximity to the IT (Fig. 1F-G). Thus, the
127 plant nucleus not only guides the progression of ITs but also establishes close physical
128 interactions with them. Overall, drastic, cell-specific ultrastructural changes take place in
129 outer cortical cells primed for rhizobia infection, which are marked by a unique transcellular
130 cytoplasmic organization, enriched with ER, small vacuole-like structures and perinuclear
131 mitochondria.

132

133 ### MtAnn1 and Ca^{2+} spiking dynamics mark symbiotically engaged and infected plant cells

134 *MtAnn1*, encoding a Ca^{2+} and membrane phospholipid binding annexin protein, is
135 expressed in outer cortical cells preparing for rhizobia infection[13], where coincidently Ca^{2+}
136 spiking responses are transiently regulated[42]. To assess if these two responses are functionally
137 interconnected, we set up a new *in vivo* strategy aimed at monitoring both responses
138 simultaneously in individual root cells. Co-expression of a red fluorescent NR-GECO1 nuclear
139 calcium sensor[44] and a green fluorescent MtAnn1-GFP fusion was therefore used to live track
140 the spatio-temporal dynamics of Ca^{2+} spiking and MtAnn1 in (i) non-infected, Nod factor-
141 responsive root hairs of the nodulation susceptible zone, (ii) infected root hairs in the proximal
142 root region and (iii) adjacent primed cortical cells. These challenging analyses were performed
143 in *M. truncatula* A17 (wild-type, WT) and in the *sunn2* mutant[45]. This mutant, which shows
144 wild-type infection events but in greater numbers, is optimal for live imaging studies of early
145 rhizobia infection events[24,27,46].

146 Periodic, high frequency, Ca^{2+} oscillations resembling those induced by purified Nod
147 factors[44], are observed in most root hairs of the nodulation susceptible zone as early as 12 h
148 post-inoculation with *Rhizobia* in both *sunn2* and A17 (Supplementary Fig. S1 and Movies 1-2
149 show control and rhizobia-inoculated WT root hairs at 1 dpi). Double labelling of MtAnn1-GFP
150 and NR-GECO greatly facilitated detection of root hairs in early stages of bacterial entrapment
151 (RHE) and IT polar growth. Indeed, infected root hairs show both Ca^{2+} spikes and MtAnn1-GFP
152 fusion expression (Fig. 2). However, MtAnn1-GFP expression levels were clearly higher in root
153 hairs containing growing ITs compared with RHE root hairs (Fig. 2A-B). On the other hand, the
154 amplitude of Ca^{2+} spikes drops significantly in IT compared to RHE stages (Fig. 2C-E), while Ca^{2+}

155 spiking frequency is not significantly altered (Fig. 2F). Overall, our data show that a decrease
156 in Ca^{2+} spiking amplitude and a rise in MtAnn1 expression are associated with polar IT growth.

157 In addition to accompanying rhizobial entry in root hairs, MtAnn1-GFP fusion expression is
158 also observed in outer cortical cells adjacent to a root hair infection site at 3-4 dpi with rhizobia
159 (Fig. 3A-C). This labelling is specific to one or a few cells around the infection site (Fig. 3A-C).
160 Strikingly, these MtAnn1-labelled cells consistently show low frequency Ca^{2+} spiking, whereas
161 nearby cells not labelled with MtAnn1 do not show any Ca^{2+} spiking (Compare C1a-c in Fig. 3).
162 This data establishes a direct link between symbiotic priming, MtAnn1 expression and low
163 frequency Ca^{2+} spikes. Together, this data indicates that priming for infection and IT
164 development are guided by cell type and stage-specific Ca^{2+} spiking signatures that are closely
165 linked with MtAnn1 dynamics.

166

167 **Rhizobia root hair entrapment is required for pre-infection priming of adjacent cortical cells**

168 MtAnn1-GFP labelling and Ca^{2+} spiking mark symbiotically primed outer cortical cells (C1 in
169 Fig. 3C), however it is unclear if formation of a root hair IT is required before these responses
170 are activated. To gain insight into the genetic components underlying pre-infection priming,
171 we studied how these responses are triggered in IT-defective plant mutants transformed with
172 NR-GECO1 and/or the MtAnn1-GFP fusion.

173 The *M. truncatula ern1* (for ERF Required for Nodulation 1) mutant is defective in IT
174 development in root hairs, but is still able to form root hair infection chambers with entrapped
175 bacteria[47,48]. This mutant shows Ca^{2+} spiking and cytoplasmic-bridge formation (visualized with
176 MtAnn1-GFP) in early infected root hairs (Fig. 3D and Supplementary Fig. S2A and D). Pre-
177 infection priming in cells adjacent to an infected root hair site is also well visualized in this
178 mutant. Indeed, primed cells, with characteristic cytoplasmic strands radiating from the
179 central nucleus, marked with MtAnn1-GFP fluorescence and showing Ca^{2+} spiking responses,
180 are clearly distinguished in *ern1* (Fig. 3D and Supplementary Fig. S2B-D). Thus, despite being
181 defective in root hair IT growth, priming of neighbouring cells is still triggered in *ern1.*
182 However, while pre-infection priming is limited to a few adjacent cortical cells in WT and *sunn2*
183 backgrounds, it is strikingly deregulated in *ern1* (Fig. 3 and Supplementary Fig S2B-C). Priming
184 responses in *ern1* are exaggerated as they are seen in extended regions of MtAnn1-GFP-
185 labelled epidermal and cortical cells. These cells show coordinated low frequency Ca^{2+} spiking
186 (as in the WT background, Fig. 3) or unusual high-frequency patterns (Supplementary Fig 2C-
187 D). This suggests that ERN1 is not required for promoting pre-infection priming, but is
188 somehow required to spatially restrict it.

189 The *ern1 ern2*[48] and *dmi3*[8] mutants, which are totally deficient in root hair bacterial
190 entrapment and infection, show Ca^{2+} spiking in root hairs ([49] and Supplementary Fig S2E and
191 Movie 3) but no clear signs of cytoplasmic remodelling in root hairs or cortical cells. Moreover,
192 these root hairs show only residual (in *ern1 ern2*) or no (in *dmi3*) MtAnn1-GFP expression.
193 Thus, the formation of MtAnn1-labelled cytoplasmic bridges, characteristic of primed cells,
194 seems to require the formation of rhizobia root hair infection foci. To test this hypothesis, we
195 investigated if complementation of *dmi3* with a epidermal-expressed (*pEXT:DMI3*) fusion, that
196 can rescue IT development in *dmi3* root hairs[50], could restore cytoplasmic bridge formation.
197 While MtAnn1-labelled cytoplasmic bridges were strongly detected in infected root hairs of
198 complemented *dmi3*, no pre-infection priming events were observed in adjacent cortical cells

199 (no signs of MtAnn1 labelling, Ca^{2+} spiking or cytoplasmic remodelling, Supplementary Fig S2E-
200 F). This suggests that PIT-related infection priming uses a DMI3-dependent signalling pathway.

201 Overall, our mutant analyses indicate that the formation of rhizobia infection foci in root
202 hairs is sufficient to trigger the formation of strongly MtAnn1-GFP-labelled cytoplasmic
203 bridges in root hairs and in adjacent cortex. Overactive (in *ern1*) and absent (in *dmi3*) priming
204 responses in adjacent cells are consistent with the conclusion that pre-infection priming is
205 genetically-dependent on DMI3, and under tight spatial control by ERN1.

206

207 **NIN controls pre-infection priming and the associated expression of *MtAnn1***

208 The master symbiotic transcription factor Nodule INception (NIN) is genetically placed
209 downstream of DMI3 and its mutation abolishes rhizobia-induced *MtAnn1* expression[51],
210 raising the question of its implication in *MtAnn1* regulation and pre-infection priming. To test
211 if NIN is indeed required for symbiotic *MtAnn1* expression, we compared the spatio-temporal
212 expression profile of a *pMtAnn1:GUS* fusion in WT and *nin* genetic backgrounds. As shown in
213 Fig. 4A-C, strong expression of the *pMtAnn1:GUS* fusion is observed at rhizobia infection sites
214 in WT but not in *nin* roots, confirming the genetic dependence on NIN to confer infection-
215 related *MtAnn1* expression. Conversely, expression of NIN under the epidermis-specific
216 *pEXPA* promoter[52] in *nin* induces *pMtAnn1:GUS* fusion expression in the epidermis in the
217 absence of rhizobia (Fig. 4D). This indicates that NIN can bypass early symbiotic signal
218 transduction to directly activate the *pMtAnn1:GUS* fusion. Transactivation studies in *Nicotiana*
219 *benthamiana* cells (Fig. 4E and Supplementary Fig. S3), confirmed the ability of NIN to
220 transcriptionally activate the *pMtAnn1:GUS* fusion (Fig. 4E). This activation is no longer
221 observed when NIN is deleted in its DNA binding domain (Fig. 4E). These data establish NIN as
222 a likely direct regulator of *MtAnn1*.

223 Besides abolishing *MtAnn1* expression, *nin* fails to form proper infection chamber and ITs
224 but can still entrap rhizobia within a deformed root hair[24]. However, it is unclear if PIT-like
225 cytoplasmic remodelling can still be initiated in *nin*. To investigate that, the *in vivo* dynamics
226 of a fluorescent GFP-ER fusion was live tracked in *nin* complemented or not in the epidermis
227 by the expression of a *pEXPA:NIN* construct (Fig. 4F-K). In *nin*, the GFP-ER fluorescent fusion
228 marks the ER network and associated cytoplasm, mainly visualized around the nuclei and in
229 growing root hair tips. However, no cytoplasmic columns are detected in this genetic
230 background (Fig. 4F). *pEXPA:NIN*-complemented *nin* root hairs, recognized by red fluorescent
231 Ds-Red nuclei, show thick GFP-labelled cytoplasmic columns in infection chamber-forming
232 root hairs (Fig. 4G-H). However, outer cortical cells from *nin* (complemented or not) show no
233 signs of priming, as evidenced by the absence of GFP-ER or Ds-Red-labelled associated
234 cytoplasmic remodelling (Fig. 4I-K). This suggests that a functionally active NIN is required in
235 the cortex to trigger infection-related cytoplasmic remodelling. Taken together, these data
236 suggest that NIN acts downstream of DMI3 to control pre-infection priming and the associated
237 expression of *MtAnn1*.

238

239 ***MtAnn1* mutation impacts nodule differentiation and function**

240 To evaluate the relative importance of *MtAnn1* for nodulation, phenotypic analyses of
241 three available *M. truncatula Tnt1* R108 insertion mutant lines were undertaken
242 (Supplementary Fig. S4A). These lines, containing insertions in the promoter (*ann1-1*) or

243 exonic regions of *MtAnn1* (*ann1-2* and *ann1-3*), show reduced (*ann1-1*) or almost abolished
244 (*ann1-2* and *ann1-3*) rhizobia-induced expression of *MtAnn1* compared with WT lines (the
245 R108 background and WT siblings from the same mutagenized population) (Supplementary
246 Fig. S4B). Phenotyping of *ann1-2* and *ann1-3* did not reveal any major changes in root
247 architecture or nodule number compared with the WT lines at 21 dpi (Supplementary Fig. S4C-
248 F). However, nodules formed in mutant roots showed striking variations in their shape (less
249 elongated overall) and colour (paler pink) (Fig. 5A-C and Supplementary Fig. S4D-F),
250 reminiscent of potential differentiation and/or nitrogen fixation defects[53]. Indeed,
251 comparison of nodule shape in *ann1-3* and WT, by calculating the length to width ratio of
252 individual 21 dpi nodules, revealed significant differences between the two genotypes (Fig.
253 5D). An automated Image J quantification system (see Methods) confirmed nodule size
254 differences in the *ann1-2* and *ann1-3* mutants compared with WT lines at 10 dpi (Fig. 5E).

255 To better understand why *ann1* mutant nodules were smaller and less elongated, we
256 performed a detailed analysis of thin and ultrathin sections of WT and *ann1-3* nodules (Fig.
257 5G-N). Meristematic (I), infection (II), amyloplast-rich interzone (IZ) and nitrogen fixation (III)
258 zones are clearly distinguished in WT nodules (Fig. 5G and I). However, *ann1-3* nodules show
259 an abnormally large IZ like region, with over-accumulation of amyloplasts and less clearly
260 defined zone III (Fig. 5H and J). TEM analyses showed that zone III of WT nodules comprised,
261 as expected, uninvaded cells (UC) interspersed with invaded cells (IC) filled with nitrogen-fixing
262 bacteroids, the latter with low numbers of amyloplast grains located near intercellular spaces
263 (Fig. 5K and M). Although *ann1-3* nodules include IC cells with apparent differentiated
264 bacteroids (Fig. 5L, N), they comprise small vesicles (asterisks in Fig. 5N) that are normally
265 found in IZ rather than zone III of WT nodules[54]. This supports the general conclusion that
266 *ann1-3* nodules are unable to differentiate effectively into a fully functional nodule with a
267 defined zone III. As a result, *Mtann1* mutant nodules have decreased nitrogen fixation abilities
268 (Fig. 5F), which ultimately results in slightly reduced plant growth (Supplementary Fig. S4D).
269 The amyloplast-related phenotype of *ann1-3* is linked to increased expression of a gene
270 encoding an interzone-associated starch synthase, and this phenotype can be partially
271 restored in complemented roots (Supplementary Fig. S5). These results imply that starch
272 accumulated during early stages of nodule development is not properly metabolized in
273 *MtAnn1* mutant nodules. Taken together, these results indicate that *Mtann1* mutant nodules
274 are affected in their ability to differentiate and fix nitrogen.

275

276 **MtAnn1-dependent modulation of Ca^{2+} spiking and cytoplasmic ultrastructural organization**
277 **for efficient rhizobia infection**

278 As *MtAnn1* expression is tightly associated with early stages of rhizobial entry, we aimed to
279 determine the impact of *MtAnn1* mutation in rhizobial infection. We assessed this by
280 monitoring bacterial β-galactosidase reporter activity (in blue) in inoculated root and nodule
281 tissues. Root hair ITs are formed in mutant roots at 4 dpi with rhizobia, but at a lower
282 frequency compared with WT (Fig. 6A). A lower proportion also reach the outer cortex (OC)
283 and fully colonize emerging nodule primordia (NP) or nodules at 4 and 10 dpi with rhizobia
284 (Fig. 6B-K). Mutant nodule primordia are often colonized by multiple ITs compared with the
285 control (Fig. 6D-E and J), suggesting an inefficient process. Complementary RNAi knockdown
286 of *MtAnn1* in *M. truncatula* A17 also results in reduced nodule primordia colonization at 5 dpi
287 with rhizobia (Supplementary Fig. S6). Thus, impaired *MtAnn1* function in mutant and RNAi
288 contexts affects rhizobia root and nodule infection in different *M. truncatula* genotypes.

289 As Ca^{2+} spiking and MtAnn1 dynamics are closely linked in peri-nuclear regions of primed
290 cells (Fig. 2-3), we decided to assess if *MtAnn1* mutation could somehow impact symbiotic
291 Ca^{2+} spiking. WT and *ann1-3* transgenic roots expressing the NR-GECO1 Ca^{2+} sensor, were used
292 to monitor these responses. Although more challenging than previous live analysis in the
293 hyperinfectious *sunn2* context (Fig. 2), we observed the same drop in Ca^{2+} spiking amplitude
294 in IT-containing RHs compared with RHE root hairs in the WT context (Fig. 7A). However, this
295 decrease is no longer observed in *ann1* mutants (Fig. 7B). Likewise, a deregulated Ca^{2+} spiking
296 amplitude pattern is also observed in *S. meliloti*-responsive root hairs of *ann1-3* compared
297 with WT while Ca^{2+} spiking frequency is not significantly changed in any root hair categories
298 (Fig. 7C and Supplementary Fig. S7). Together, these data indicate that *MtAnn1* is required for
299 modulating symbiotic Ca^{2+} spiking responses.

300 Ca^{2+} spiking and MtAnn1 dynamics accompany cytoplasmic bridge formation (Fig. 2-3), so
301 we wondered how *MtAnn1* mutation and deregulated Ca^{2+} spiking amplitude in *ann1-3* (Fig.
302 7) could affect cytoplasmic bridge formation. We thus analysed the cytoplasmic composition
303 of infected cells in apical nodule zones of WT and *ann1-3* by resolutive TEM. As similarly shown
304 in A17 (Fig. 1), ITs in R108 WT progress through a small vacuole-like enriched cytoplasmic
305 bridge comprising a dense ER network (Fig. 7D-E and H-I). In *ann-1-3*, this small vacuole-like
306 and ER-rich environment is no longer observed in the cytoplasmic compartment around the IT
307 (Fig. 7F-G and J-K). Thus, mutation in *MtAnn1* results in a deregulated Ca^{2+} spiking response
308 and a change in the ER and vesicle composition of the remodelled cytoplasmic bridge. We thus
309 hypothesise that MtAnn1, as a calcium and membrane binding cytoplasmic annexin protein,
310 is required to modulate Ca^{2+} spiking signatures, likely needed to structurally organize the
311 cytoplasmic bridge for proper IT progression.

312

313 **_MtAnn1_ is required for proper mycorrhizal root colonization**

314 Recently developed genomic and transcriptomic databases from around 300 plant species
315 establishing different types of endosymbioses make it now possible to address key
316 endosymbiosis-related ancestral gene functions[55]. We have thus exploited these extensive
317 resources to trace the evolutionary history of *MtAnn1*. Previous studies of the monophyletic
318 plant annexin group, mainly composed of angiosperm sequences, suggested their emergence
319 through duplications from a common ancestor prior to the monocots/eudicots split[56].
320 Consistent with these data, we found that the *MtAnn1* annexin cluster likely arose from
321 sequential pre-angiosperms, eudicots and Papilionoideae-specific duplications
322 (Supplementary Fig S8). *MtAnn1* belongs to one of the Papilionoideae duplicated clades,
323 which includes mainly species that establish intracellular endosymbioses (Supplementary Fig.
324 S8), with the exception of *Caryophyallae* and *Cephalotus* (status uncertain). In particular, *Ann1*
325 orthologs were also detected in Papilionoideae species that have lost RNS but maintain the
326 AM symbiosis. This indicates that the function of *Ann1* is not restricted to RNS but could
327 expand to the AM symbiosis. Strikingly, *MtAnn1* from different species show consistent
328 transcriptional activation during both root nodule symbiosis and the ancient AM symbiosis,
329 suggesting an ancestral role in root endosymbiotic infection[4]. To determine if this was the
330 case, we first decided to assess if *MtAnn1* promoter activity was spatio-temporally regulated
331 in *M. truncatula* roots colonized by the AM fungus *Rhizophagus irregularis*. Strong activation
332 of a *pMtAnn1:GUS* fusion was observed in root segments colonized by *R. irregularis* at 4 wpi,

333 especially in cortical cells containing arbuscules (Fig. 8A-B), consistent with an important role
334 for *MtAnn1* in AM symbiosis development. To assess that, we compared the percent root
335 length colonization of WT and *ann1-3* mutant roots colonized by *R. irregularis*. At 6 wpi, WT
336 roots showed, as expected, root segments densely colonized by *R. irregularis*, with cortical
337 cells fully filled with arbuscules (Fig. 8C, E and F). The mutant roots, on the other hand, were
338 significantly less colonized (Fig. 8C, G and H). They not only had a lower proportion of
339 colonized root sectors (Fig. 8C), but the arbuscule density was also reduced (Fig. 8D). These
340 data highlight the involvement of *MtAnn1* in the ancient AM symbiosis and suggest its
341 ancestral recruitment for successful colonization by endosymbiotic microbes.

342

343 ## Discussion

344 Endosymbiotic root infection by rhizobia occurs in most legumes transcellularly, through
345 the creation of IT apoplastic structures that grow polarly to reach the developing nodule. Plant
346 cells engage symbiotically in this process by creating characteristic trans-vacuolar PIT
347 cytoplasmic bridges, which shape the cellular route for IT progression. PITs, along with
348 analogous PPA structures formed during infection by AM fungi, are likely governed by
349 common ancestral cellular mechanisms, though knowledge remains limited to date. In this
350 manuscript, we uncover cell-specific ultrastructural rearrangements and stage and cell-
351 specific Ca^{2+} responses that prime *M. truncatula* plant cells for endosymbiotic infection by
352 rhizobia. We show that pre-infection reprogramming is marked by an intimate link between
353 Ca^{2+} spiking and the annexin MtAnn1, which together integrate the so-called primed cellular
354 state, induced in dependence of a DMI3-NIN-controlled genetic pathway. We discovered
355 MtAnn1 as a novel regulator of symbiotic Ca^{2+} spiking amplitude. Also, MtAnn1 plays an
356 important role in the creation of a dense, ER- and small vacuole-rich cytoplasmic environment,
357 propitious for successful rhizobial infection. This study also shows that *MtAnn1* is needed for
358 successful formation of nitrogen-fixing nodules by rhizobia and root cortical arbuscules by AM
359 fungi. Alongside the ancient recruitment of *MtAnn1* in plants establishing endosymbioses,
360 experimental evidence from this work suggests the functional importance of *MtAnn1* in
361 driving efficient Ca^{2+}-regulated trans-vascuolar cytoplasmic bridge formation for successful
362 endosymbiotic root infection.

363

364 **Organelle dynamics shaping rhizobia pre-infection priming**

365 Dissecting the ultrastructure of plant cells preparing for transcellular rhizobia infection
366 revealed the marked enrichment and spatial re-distribution of organelles during this process
367 (Fig. 1). This pre-infection priming state is only visible in a few outer cortical cells prior to IT
368 entry (Fig. 1 and 3), underlining a tight cell-specific regulatory control. As reported during PPA
369 formation[33], mitochondria enrichment is observed in these primed cells (Fig. 1), perhaps
370 reflecting the highly energy-demanding nature of these processes. Nevertheless, perinuclear
371 clustering of mitochondria is not prevalent in surrounding root cells, not even in C3
372 meristematic cells with presumably high metabolic activity (Fig. 1). Of note, the distribution
373 of mitochondria around the nucleus appears to be dynamically regulated during cell cycle
374 transitions in *A. thaliana*[57]. As cells undergoing or preparing for rhizobia infection are under
375 tight cell cycle control[37,39], this mitochondrial pattern may reflect a unique cell-cycle activation
376 status of primed cells. Mitochondria perinuclear clustering could also simply reflect the dense

377 cytoplasmic clustering around the nucleus. Nevertheless, as mitochondria play emerging roles
378 in modulating cytoplasmic Ca^{2+}signals in plants[58], it is tempting to speculate if their clustering
379 in the perinuclear region, where dynamic calcium oscillations occur, could have regulatory
380 implications in the symbiotic Ca^{2+} response.

381 Previous studies showed that the transcellular cytoplasm of rhizobia primed cells is shaped
382 by microtubule bundles and decorated by an ER network[38,40,41]. Our TEM analysis provided
383 ultrastructural evidence that a dense ER-rich network occupies the transcellular cytoplasmic
384 bridge in *M. truncatula* root cells either primed or rhizobia infected (Fig. 1 and Fig. 7). This
385 region is also rich in small vacuole-like structures, but we cannot definitely determine if these
386 are fragmented or small, newly-formed, vacuoles[59]. Also, we were unable to detect an
387 enrichment in multivesicular bodies (MVBs) seen in PPA[60] perhaps masked by the prominent
388 vacuoles. Nevertheless, a functional link may exist here as small vacuoles can derive from MVB
389 fusion[59]. Small vacuole-like structures are also observed in PPA, in dividing cells or sub-apical
390 regions of growing root hairs[59,60,75]. As the ER represents the gateway to intracellular
391 trafficking and the main source for vacuole biogenesis[61], the ER and small vacuole-enriched
392 pattern of primed cells is suggestive of an active vesicle fusion and/or vacuole biogenesis
393 process, in which the annexin MtAnn1 appears to be an important component, as discussed
394 hereafter.

395

396 **Role of MtAnn1 in modulating cell- and stage-specific symbiotic Ca^{2+} responses**

397 High frequency Ca^{2+} spiking, triggered by Nod factors in root hairs of the nodulation
398 competence zone, is central for early recognition of rhizobia[5,6,44]. Here, we showed that a
399 second Ca^{2+} spiking phase occurs in root hairs undergoing rhizobia infection, and involves a
400 decrease in Ca^{2+} peak amplitude as ITs extend into root hairs (Fig. 2). This drop was also
401 reported to occur in root cortical cells crossed by an IT[42], consistent with the hypothesis that
402 this regulatory switch is key for IT progression in the cell. Regulation of Ca^{2+} amplitude is
403 known to finetune different biological processes, from gene expression regulation, stomatal
404 closure to gravitropic response, and even synaptic plasticity in animals[62-64]. The deregulated
405 Ca^{2+} amplitude profile and defective infection caused by *MtAnn1* mutation (Fig. 6 and 7)
406 supports the need for such a strict control and establish a direct functional link between
407 MtAnn1 and the regulation of Ca^{2+} spiking amplitude during rhizobia infection.

408 Symbiotic Ca^{2+} spiking is generated in the nucleoplasm and perinuclear cytoplasm in
409 *Medicago* by the concerted action of nuclear envelope ion channels (DMI1, CNGC15), a Ca^{2+}
410 pump (MCA8), and under negative feedback regulation by a nuclear calmodulin (CaM2)[5,65].
411 MtAnn1, as a cytosolic protein, is unlikely to be among the top Ca^{2+} spike-generating proteins,
412 but clearly contributes to moderate the signal amplitude. MtAnn1 is a phospholipid- and Ca^{2+}-
413 interacting protein of the annexin family[13], viewed as dynamic cytosolic regulators that
414 associate to membranes when intracellular Ca^{2+} levels change[15]. Members of the annexin
415 family have been implicated in the regulation of ion transport, modulation of cytoplasmic Ca^{2+}
416 signals and ROS signalling in diverse abiotic or biotic responses[16-19,66]. Even though annexins
417 are predominantly cytoplasmic, they can also topologically associate with the ER[67,68] and
418 modulate the activity of Ca^{2+}-release channels[69]. As MtAnn1 seems to partially co-localize with
419 the peri-nuclear ER network in symbiotically activated cells, it could mechanistically play such
420 a regulatory role, which would explain the disturbed Ca^{2+} signals and ER phenotypes caused
421 by the *MtAnn1* mutation.

422 We determined that Ca^{2+} spiking and strong MtAnn1-GFP labelling are hallmarks of rhizobia
423 pre-infection priming (Fig. 3) and rely on cell-autonomous activity of DMI3, as PPA
424 formation[35,43] and NIN. These findings corroborate that spatially distinct Ca^{2+} spiking
425 responses are triggered, first by Nod-factors in non-infected root hairs independently of DMI3-
426 NIN, before infection-related Ca^{2+} spiking is induced in a DMI3-NIN-dependent fashion in cells
427 engaged for infection. The latter appears to require successful infection chamber formation
428 (seen in *ern1* not in *ern1 ern2*, *dmi3*, *nin*, Fig 3), supporting the hypothesis that rhizobia
429 entrapment and proliferation in the chamber are pre-requisites for pre-infection priming.
430 Moreover, ERN1 spatially restricts this process to a few cells (Fig. 3), perhaps key to delimiting
431 the cellular route of IT passage. In agreement with previous results[42], we observe unique low
432 frequency Ca^{2+} spiking only in primed cells of the cortex (Fig. 3). Although root hairs exhibit
433 similar remodelling and MtAnn1 labelling responses, they do not show low frequency Ca^{2+}
434 spiking. Thus, this Ca^{2+} signature is probably not reflecting a generalized commitment to
435 infection but rather a specific state of cortical cells, possibly linked to their positioning at a
436 distance from the root hair infection site.

437

438 **Functional implications of MtAnn1 in organising the dense IT-associated cytoplasmic bridge**

439 The radical alteration in the cytosolic distribution of the ER and small vacuoles by the *MtAnn1*
440 mutation (Fig. 7), establishes a strong functional link between *MtAnn1* and the generation of
441 this specific cytoplasmic configuration. Ca^{2+} orchestrates membrane trafficking and fusion,
442 while vacuoles, emitters and receivers of Ca^{2+}signals, can be directly affected by altered levels
443 of cytosolic calcium[70,71]. Pollen germination is driven by interconnected calcium oscillations
444 and exocytosis[72], so a similar scenario is conceivable in primed cells. Annexins are among Ca^{2+}
445 sensing proteins involved in endomembrane trafficking in plants[73], either acting in conjunction
446 with the membrane fusion machinery or regulating exocytosis. Thus, MtAnn1 may directly or
447 indirectly impact Ca^{2+}-regulated vesicle trafficking and/or vacuole morphology. However, the
448 biological relevance of such a dense cytoplasmic strand for IT passage remains to be
449 determined. Modulation of vacuole shape and distribution is used to optimize stomatal
450 aperture, root hair development and presumably to spatially accommodate the future cell
451 plate structure in dividing cells[74]. By analogy with the latter, dynamic shrinking of vacuoles in
452 primed cells may be used to accommodate the future passage of the IT. A parallel can also be
453 drawn with the similar reorganisation of a dense cytoplasmic region, rich in ER and small
454 vacuoles, in the subapical zone of growing root hairs, in which the dense organelle
455 arrangement appears to impact the speed of cytoplasmic streaming[75,76]. It is thus conceivable
456 that ultrastructural cytoplasmic alterations in primed cells may somehow be needed to create
457 an optimal streaming rate for IT growth.

458

459 **Evolutionary recruitment of *MtAnn1* for root endosymbioses**

460 Through analysis of insertional mutants, we demonstrated the importance of *MtAnn1* for
461 proper infection and differentiation of nitrogen fixing nodules (Fig. 5). In these mutants,
462 rhizobia root infection is reduced (Fig. 6) and this impairment culminates in mature nodules
463 with decreased size and altered shapes, reminiscent of the reduced infection levels and nodule
464 sizes observed in *Phaseolus* RNAi knock-down of *PvAnn1*[77]. Microscopy analysis also revealed
465 strong differentiation phenotypes in *MtAnn1* mutant nodules, marked by a defect in

466 differentiation of nodule zone III, enhanced starch accumulation and overall diminished
467 nitrogen fixation ability (Fig. 5). These phenotypes are probably a consequence of the early
468 deregulated Ca^{2+} spiking, impaired cytoplasmic configuration and consequently defective
469 infection caused by the *MtAnn1* mutation. During nodule primordia development, infection
470 progression must be tightly synchronized with nodule organogenesis[30]. A possible slowdown
471 of IT progression in the mutant may thus directly impact synchronization, resulting in impaired
472 nodule differentiation.

473 A striking defect in mutant nodules is the marked overproduction of amyloplasts (Fig. 5),
474 as previously observed in other nitrogen fixation defective nodules[53]. Starch is normally
475 consumed in both infected and uninfected cells to fuel the differentiation of infecting bacteria
476 into nitrogen-fixing bacteroids. This abnormal pattern, never seen in WT background, is
477 probably not due to a simple delay in the nodule differentiation process, but rather reflects
478 an irreversible defect created by *MtAnn1* mutation. The close paralogue *MtAnn2*[14] is unlikely
479 to compensate for the loss of function of *MtAnn1* in nodules, as it has a distinct spatial
480 expression profile.

481 We showed that the *MtAnn1* annexin cluster emerged mainly in plant species establishing
482 intracellular symbioses. The induced expression of *MtAnn1* in rhizobia and AM symbioses and
483 its requirement for proper formation of nitrogen-fixing nodules and cortical arbuscules (Fig. 5
484 and 8) suggest ancestral and common roles of *MtAnn1* for endosymbiotic infection. We
485 propose that *MtAnn1* fine-tunes oscillatory Ca^{2+} responses for creating an optimal dense
486 cytoplasmic environment for rhizobia IT and AM fungi hyphae progression. *MtAnn1* is
487 regulated by NIN during rhizobia symbiosis (Fig. 4), we thus hypothesize that its evolutionary
488 recruitment for nodulation involved the acquisition of putative NIN *cis*-regulatory motifs
489 which are indeed present in the *MtAnn1* promoter. As NIN is specifically involved in
490 nodulation[3], it is likely that AM-associated regulation of *MtAnn1* is mediated by another, yet
491 unidentified, regulator.

492 In conclusion, we showed that cell-specific Ca^{2+} spiking signals shape rhizobia pre-infection
493 priming to prepare the optimal dense cytoplasmic environment for IT passage in *Medicago*,
494 and MtAnn1 emerges as a key modulator of this process. MtAnn1, necessary for proper
495 nodule and AM development, was possibly recruited during evolution to integrate an
496 ancestral Ca^{2+}-regulatory module for guiding endosymbiotic root infection. MtAnn1 includes
497 a K/H/RGD motif[15], possibly interacting with C2-domain Ca^{2+}-binding proteins, and further
498 exploration of associated protein interactors should help uncover other critical components
499 in this process.

500

501 ## Methods

502 ### Plant materials and microbial strains

503 *M. truncatula* Jemalong A17 and R108 wild-type ecotypes, as well as *sunn-2*[45], *dmi3-1*[8], *nin-*
504 *1*[78] and *ern1* & *ern1 ern2*[47,48] mutants were used in this work. The *dmi3* line carrying the
505 *pEXT:DMI3* construct[50], hereafter called *dmi3 + pEXT:DMI3*, was kindly provided by C.
506 Remblière (LIPME, Toulouse). The three R108 *Tnt1* mutants carrying insertions in *MtAnn1*
507 were obtained from Oklahoma State University (details in Supplementary Fig. S4) and are
508 designated *ann1-1* (NF0830), *ann1-2* (NF17737) and *ann1-3* (NF4963). These lines were self-
509 crossed and genotyped by PCR and sequencing at each generation using primers *-344*

510 *pMtAnn1-Fw*, *Mtr14183-Rev*, -914 *pMtAnn1-Fw*, *LTR6-* and *LTR4-* (Supplementary Table S1).
511 Homozygous mutants and sibling wild-type lines (referred to as WT) were selected for seed
512 multiplication and phenotyping. WT used in Fig. 5 to 8 are WT siblings derived from line
513 NF4963. Seeds were scarified and surface-sterilized prior to germination on inverted soft agar
514 plates[46] and used for *A. rhizogenes* transformation or nodulation experiments. *N.*
515 *benthamiana* seeds were germinated in potting soil in glass-covered trays before transfer to
516 pots (7 cm x 7 cm x 6.5 cm) at 21°C in a growth chamber under a 16h photoperiod and 70
517 µE/m/s light intensity for 3 weeks until bacterial infiltration. The strains *A. rhizogenes* ARquA1,
518 *A. tumefaciens* GV3103 & GV3101 and *S. meliloti* 2011 (*Sm*2011-lac), constitutively expressing
519 a *hemA-lacZ* fusion, were described[46]. The *S. meliloti* 2011 strain *Sm*2011-cCFP, constitutively
520 expressing a cyan fluorescent protein was kindly provided by P. Smit, Wageningen (The
521 Netherlands). *R. irregularis* spores (DAOM197198) were purchased from Agronutrition
522 (Labège, France).

523

524 **DNA constructs**

525 *pMtAnn1:MtAnn1-GFP*[13] and *pENOD11:GFP-ER*[41] in pBIN121 were used to study live pre-
526 infection priming responses in *M. truncatula*. *p2x35S:NR-GECO1* in pCAMBIA-CR1ΔDs-Red[44]
527 was used to monitor Ca^{2+} spiking in *M. truncatula*. *pMtAnn1:GUS* in pLP100[13], *pEXPA:NIN* in
528 pK7WG2-R*, p35S:3xHA-NIN* and *p35S:3xHA-NINΔ* in PAM-PAT35S-3xHA-GTW[52], were used in
529 transcription activation studies in *M. truncatula* or *N. benthamiana*. *p35S:MtAnn1-GFP* and
530 *p35S:GFP* in pBIN121[13], were used in mutant complementation studies. The *pMtAnn1:RNAi-*
531 *MtAnn1* and *pMtAnn1:GUS* (control) constructs were generated here by Golden-Gate cloning
532 into the pCambia-CR1 vector[44]. Briefly, DNA fragments corresponding to 2,2 kb *MtAnn1*
533 sequences upstream of the ATG, 942 bp of *MtAnn1* coding sequence in sense and antisense
534 orientations and the GUS coding sequence, were generated by PCR amplification using the
535 primer pairs *pMtAnn1-GG-A-Fw*/*pMtAnn1-GG-B-Rev*, *MtAnn1-ATG-GG-B-Fw*/*MtAnn1-STOP-*
536 *GG-C-Rev*, *MtAnn1 antisens-STOP-GG-X-Fw*/*MtAnn1 antisens-ATG-GG-D-Rev* and *GUS-GG-B-*
537 *Fw*/*GUS-GG-D-Rev*, respectively (Supplementary Table S1). DNA fragments were then cloned
538 into a pBluescript SK vector and validated by DNA sequencing prior to Golden Gate assembly.
539 Golden-Gate reactions with plasmids comprising (i) the *MtAnn1* promoter, *MtAnn1* coding
540 sequences (sense and antisense) and a 1,3 kb intron spacer[29] or (ii) the *MtAnn1* promoter and
541 the *GUS* coding sequence, were used to generate *MtAnn1* RNAi (*pMtAnn1:MtAnn1 sens-*
542 *intron-MtAnn1 antisens*) or GUS control (*pMtAnn1:GUS*) constructs in the binary pCambia-CR
543 vector. All binary vectors used for *A. rhizogenes* transformation of *M. truncatula* (pLP100,
544 pCambia, pK7WG2-R, pBIN121) include a kanamycin resistance cassette in the T-DNA region.
545 pK7G2-R and pCambia-CR1 vectors also include a Ds-Red cassette.

546

547 **Generation of *M. truncatula* transgenic material**

548 *A. rhizogenes*-mediated transformation of *M. truncatula* A17 (WT, *sunn-2*, *ern1*, *ern1 ern2* and
549 *dmi3*) or R108 (WT sibling and *ann1-3*) was performed as described[46]. Briefly, germinated
550 seedlings had their root tips removed with a scalpel and were placed on Fahraeus medium
551 plates (12 cm x 12 cm) supplemented with 0.5 mM NH_4NO_3 and 20 mg/L kanamycin, before
552 inoculation with a drop (~3 µL) of *A. rhizogenes* aqueous suspension (OD_{600nm} 0.5). For co-
553 transformation experiments with strains *pMtAnn1:MtAnn1-GFP + p2x35S:NR-GECO1,*
554 *p2x35S:NR-GECO1 + pENOD11:GFP-ER, pEXPA:NIN + pENOD11:GFP-ER or pEXPA:NIN +*

555 *pMtAnn1:GUS* (in pLP100), equal volumes of bacterial suspensions were mixed prior to
556 seedling inoculation. The lower ¾ part of the plates were sealed with parafilm and placed
557 vertically in plastic boxes under controlled 16h light/ 8h dark photoperiod conditions, first at
558 20°C for 1 week, then at 25°C for two to three weeks. Composite *M. truncatula* plants with
559 kanamycin resistant roots were selected. In some experiments, kanamycin-resistant
560 composite roots were re-selected on the basis of constitutive fluorescence of the Ds-Red
561 marker (for pK7WG2-R *pEXPA:NIN* and pCAMBIA-CR1 *pMtAnn1:RNAi-MtAnn1* and
562 *pMtAnn1:GUS* constructs), fusion fluorescence in lateral roots (for *pMtAnn1:MtAnn1-GFP* and
563 *pENOD11:GFP-ER* constructs) or in the nucleus (for *p2x35S:NR-GECO1*). Selected composite
564 plants were then transferred to appropriate nitrogen- and antibiotic-free plates or pots for
565 subsequent microbial inoculation.

566

567 **Plant growth and microbial inoculation procedures**

568 For *in vivo* imaging experiments, kanamycin-resistant and fluorescent-positive composite
569 plants of A17 (WT, *sunn-2*, *ern1*, *ern1 ern2* and *dmi3*) or R108 (WT sibling and *ann1-3*) carrying
570 *pMtAnn1:MtAnn1-GFP* + *p2x35S:NR-GECO1, pEXPA:NIN* + *pENOD11:GFP-ER* or *p2x35S:NR-*
571 *GECO1* + *pENOD11:GFP-ER* constructs were transferred to nitrogen-free Fahraeus plates
572 supplemented with Amoxycillin sodium/Clavulanate potassium 5:1 (200 mg/L) for 3-7 d, then
573 transferred to nitrogen-free 0.5% [w/v] phytagel Fahraeus plates supplemented with 50nM 2-
574 amino ethoxyvinyl glycine (AVG) for 3 d as described previously[24]. Whole root systems were
575 then inoculated with 0.5 to 1 mL of the *Sm*2011-cCFP suspension (OD_{600nm} 0.001), applied
576 between the medium and the LUMOX film. The inoculated root systems were kept protected
577 from light, by wrapping ¾ of the plates with dark plastic bags in a culture room at 20°C or 25°C
578 with a 16-h photoperiod and a light intensity of 70 mE/s/m^2, until microscopy observations.

579 For high-resolution microscopy analyses of pre-infection priming in A17 and nodule
580 differentiation in WT/*ann-3*, germinated seedlings of *M. truncatula* A17 and R108 (WT sibling
581 and *ann1-3*) were grown for 3 days on nitrogen-free paper/Fahraeus Kalys HP696 agar plates[46]
582 before roots were spot or flood-inoculated with water (control) or a *Sm*2011-LacZ (OD_{600nm}
583 0.01) suspension, as described in[29]. For expression analyses of *pMtAnn1:GUS* (in pLP100) in
584 A17 and *nin* (co-expressing or not *pEXPA:NIN*), kanamycin-resistant and/or Ds-Red
585 fluorescence-positive composite plants were transferred 3 weeks after *A. rhizogenes*
586 transformation to the same nitrogen-free paper/Fahraeus Kalys HP696 agar plates and grown
587 for 3 days prior to flood inoculation (for 1h) of the entire root system with *Sm*2011-LacZ
588 (OD_{600nm} 0.01). Plants grown *in vitro* on plates were all cultivated at 25°C under a 16-h
589 photoperiod and a light intensity of 70 mE/s/m^2 with their root systems protected from light
590 by wrapping ¾ of the plates with dark plastic bags.

591 For phenotyping experiments, germinated seedlings of *M. truncatula* R108 lines (R108, WT
592 sibling and *ann1-1 to ann1-3* mutants), and selected composite plants (2-3 weeks after
593 transformation) of A17-transformed with MtAnn1-RNAi/control constructs or R108 (WT or
594 *ann1-3*)-transformed with *p35S:GFP/p35S:MtAnn1-GFP* constructs, were transferred to 8 x 8
595 x 7cm pots (3 plants/pot for germinated seedlings and 2 plants/pot for composite plants) filled
596 with inert attapulgite substrate (Oil Dri US Special; http://www.oildri.com/), supplemented
597 with 10mL nitrogen-free Fahraeus medium. For longer growth periods (> 3 wpi), plants were
598 grown in 9 x 9 x 8 cm pots (3 plants/pot) supplemented with 14mL medium. Pots were placed
599 in small greenhouses at 25°C, with a 16 h photoperiod and a light intensity of 100 mE/s/m^2,

600 and inoculated with a suspension of *Sm*2011-LacZ (OD_{600nm} 0.1), after 3 days of nitrogen
601 starvation.

602 To assess mycorrhizal root colonization of WT and *ann1-3* mutant lines, germinated seedlings
603 were transferred to 8 x 8 x 7cm pots (1 plant per pot), filled with a 1:1 mix of Zeolite substrate
604 fractions 1.0-2.5 mm and 0.5-1.0 mm (Symbiom LTD, Lanskroun, Czech Republic), and
605 inoculated with *R. irregularis* spores (strain DAOM197198, 150 spores per pot). Pots were
606 placed in 60 x 40 x 12 cm trays in a 16 h photoperiod chamber (light intensity: 300 µmol m^{-2} s^{-}
607 ^{1}) at a day-time temperature of 22 °C day and a night-time temperature of 20°C and 70%
608 humidity. Plants were watered weekly with a modified low-phosphate and low-nitrogen Long
609 Ashton solution (7.5 µM Na_2HPO_4, 750 µM KNO_3, 400 µM $Ca(NO_3)_2$, 200 mg/L MES buffer, pH
610 6.5).

611

612 **β-glucuronidase (GUS) and β-galactosidase enzymatic assays**

613 Root segments from *M. truncatula* composite plants expressing *pMtAnn1:GUS* (in pLP100) or
614 *pEXPA:NIN + pMtAnn1:GUS* constructs were collected from control (water) or rhizobia-
615 inoculated roots and incubated in 0.5 % paraformaldehyde/0.1 M potassium phosphate buffer
616 pH 7.0, for 1 h, prior to histochemical (blue) staining for GUS activity for 2-5 hours at 37 °C
617 using 1 mM of the substrate X-Gluc (5-bromo-4-chloro-3-indoxyl-b-D-GlcA,
618 cyclohexylammonium salt, B7300; Biosynth, Staad, Switzerland) as described[48]. For
619 mycorrhizal roots expressing *pMtAnn1:GUS*, composite plants were harvested 4 weeks after
620 inoculation with *R. irregularis*. The root system was vacuum-infiltrated five times for 5 min
621 each with GUS staining solution (0.5 mg/ml X-Gluc, 100 mM phosphate buffer pH 7.0, 100 mM
622 EDTA, 0.5 mM $K_4[Fe(CN)_6]$, 0.5 mM $K_3[Fe(CN)_6]$ and 0.1% Triton X-100), and then incubated in
623 this solution for 1 h at 37 °C in the dark. Histochemical GUS staining of *N. benthamiana* leaf
624 discs was carried out in the same X-Gluc substrate but supplemented with 0,1 % triton, first
625 under vacuum for 20 min at room temperature before incubation at 37 °C for 3 h. Enzymatic
626 GUS fluorimetric assays of *N. benthamiana* leaf discs were done according to [46]. Briefly, tissues
627 were ground using a MM400 grinder (Retsch) and homogenized in GUS extraction buffer
628 before 1 µg of total protein extracts were used for enzymatic reactions at 37°C using 1 mM of
629 the 4-MUG substrate (4-Methylumbelliferyl-β-D-glucuronide hydrate, Biosynth M-5700). GUS
630 activity was measured using a FLUOstar Omega 96 microplate reader (BMG LABTECH, France)
631 through quantification of the fluorescence of 4-MU (4-Methylumbelliferone, Sigma) reaction
632 product. To reveal the constitutive β-galactosidase activity of the *S. meliloti* strain *Sm2011-*
633 *lacZ* in ITs, root samples (sometimes pre-stained for GUS activity) were rinsed and fixed for 1
634 h in 1.25 % glutaraldehyde/Z buffer (10 mM KCl, 1 mM $MgCl_2$, and 0.1 M phosphate buffer,
635 pH 7.0) as described[46]. After rinsing in Z-buffer, root samples were incubated overnight in the
636 dark at 28 °C in Z-buffer containing 2 mM Magenta-Gal (5-bromo-6-chloro-3-indoxyl-b-D-
637 galactopyranoside; B7200; Biosynth) or X-Gal (5-bromo-4-chloro-3-indolyl-b-D-
638 galactopyranoside, W5376C; Thermo Fisher Scientific, Guilford, CT). GUS and/or LacZ-stained
639 tissues were cleared for 30 s with 12 % sodium hypochlorite solution before microscopy
640 observations.

641

642 **Tissue harvesting and microscopy methods**

643 Roots of *M. truncatula* composite plants expressing different fluorescent fusions and grown
644 under LUMOX film were observed using a Leica TCS SP8 AOBS laser scanning confocal
645 microscope equipped with a 40x long distance water immersion objective (HCX APO L U-V-I
646 40x/0.80 WATER). Confocal images were recorded using Leica LAS-X software, before and
647 after rhizobia inoculation (from 1 to 7 dpi). For GFP, CFP and Ds-Red fluorescent proteins, 458
648 nm and 488 nm Argon laser lines and a 561 nm diode were used for excitation, respectively,
649 with emission windows set at 465-495 nm, 500-525 nm and 570-600 nm (hybrid detector),
650 respectively. To avoid potential interference, sequential mode was used to acquire CFP and
651 red fluorescent protein fluorescence separately from GFP fluorescence and bright-field
652 images. For confocal imaging of calcium responses, the 561 nm diode was used to excite the
653 mApple red fluorescent protein from the NR-GECO1 sensor, and the emitted fluorescence was
654 recovered using a hybrid detector in the 600 to 643 nm emission window. Time series (t-series)
655 were acquired at 5 s intervals for 10 to 15 min, with pinhole diameter set to 3 Airy units, as
656 described[44].

657 Roots or nodulated roots of *M. truncatula* A17 and R108 (WT and *ann1-3*) or composite plants
658 were selected on the basis of their fluorescence and/or analyzed before or after GUS and/or
659 β-galactosidase staining using stereomicroscopy (Leica S6E) or light microscope (AxioPlan II
660 Imaging; Carl Zeiss, Oberkochen, Germany). For *pMtAnn1:GUS* (in pLP100) expression
661 analysis, samples were harvested 0 and 4 dpi with rhizobia. For comparative phenotyping of
662 wild-type and *MtAnn1* mutant or RNAi roots, β-galactosidase stained nodulated root samples
663 were harvested 4, 5, 7, 8, 10 or 11 dpi with rhizobia. To quantify nodule size (Fig. 5E) and
664 rhizobia infection levels (Fig. 6K), β-galactosidase-stained nodulated root systems (10 dpi)
665 from WT and *ann1-3* plants were scanned (Objectscan 1600, Microtek) and the acquired
666 images (TIFF) were used for image quantification.

667 For high-resolution microscopy analyses of pre-infection priming responses in A17, control
668 roots and rhizobia-infected root regions or nodule primordia were carefully isolated 5-6 dpi in
669 fixative solution from spot-inoculated or flood-inoculated root systems (after histochemical
670 revelation of rhizobial β-galactosidase activity). Harvested root sections or nodule primordia
671 were fixed in 2% glutaraldehyde, diluted in 0.2 M cacodylate buffer pH=7.3 for a few hours at
672 room temperature or 1-3 days at 4°C, then rinsed with buffer, before progressive dehydration
673 in an ethanol series and final inclusion in LR White resin following manufacturer's instructions
674 (EMS). For comparative ultrastructural analysis of isolated WT and *ann1-3* nodules, nodule
675 samples were carefully isolated from rhizobia-inoculated root systems 14-16 dpi and fixed
676 under vacuum in 2 successive batches of 2.5% glutaraldehyde diluted in 0.2 M cacodylate
677 buffer pH=7.3, the first batch containing saponin or triton (0.1 % final) for 3-5 days at 4°C.
678 After rinsing in buffer, post-fixation in 2% osmium tetroxyde (diluted in 0.2 M sodium
679 cacodylate), rinsing again in buffer, progressive dehydration in an ethanol series and
680 incubation in propylene oxide (2 x 1h), samples were finally embedded in Epon 812 resin (EMS)
681 following the manufacturer's instructions. For all samples, semi-thin (1 µm) and ultra-thin (80
682 nm) sections were generated using an Ultracut E ultramicrotome (Reichert Jung). Semi-thin
683 sections of root/nodule primordia (5-6 dpi) were stained with basic fuchsin (0.07 % in water)
684 to help visualize ITs, while mature nodule sections (14-16 dpi) were stained in an aqueous
685 solution with methylene blue (0.2 %), toluidine blue (1 %), borax (1 %) and basic fuchsin (0.07
686 %) before observation by bright field microscopy (Axioplan II Imaging; Carl Zeiss). Ultrathin
687 sections (80 nm) were contrasted with Uranyless and lead citrate (Delta microscopy) and
688 observed using a Hitachi 7700 electron microscope (Hitachi High-Tech).

689 For histochemical GUS staining of mycorrhizal roots, selected composite plants transformed
690 with *pMtAnn1:GUS* were transferred to 7 x 7 x 8 cm pots (5 plants/pot) filled with washed
691 quartz sand (grain size 0.7-1.2 mm) pre-watered with modified half-strength Hoagland
692 solution containing 20 µM phosphate[79]. Each plant was inoculated with 500 spores of *R.*
693 *irregularis* DAOM197198 (C-grade, Agronutrition, Toulouse, France). Plants were grown in a
694 Polyklima cabinet at 22°C constant temperature, 60 % air humidity and 16-h-light/8-h-dark
695 cycles, at 200 µE m−2 s−1 light intensity and a combination of warm and cold LED 'True
696 DayLight' at a 40:25 ratio. Pots were watered twice per week with 30-40 ml of autoclaved de-
697 ionized tap water, and fertilized once per week with 30-40 ml of modified half-strength
698 Hoagland solution containing 20 µM phosphate. To visualize the fungal structures, the GUS
699 staining solution was exchanged for 10 % KOH and the roots incubated for 15 min at 95°C.
700 After KOH removal, the roots were washed 3 times with de-ionized water. After addition of
701 0.1 M HCl, the roots were further incubated for 2 h in the dark at room temperature. HCl was
702 removed and the roots were washed 3 times with de-ionized water and once with PBS. This
703 was followed by an overnight incubation at room temperature in the dark with 200 ng/µL
704 WGA Alexa Fluor 488 (Invitrogen W11261) in PBS. Roots were imaged with a LEICA DM6B
705 epifluorescence microscope. To compare the extent of mycorrhizal colonization of roots
706 between WT and *ann1-3* lines, whole root systems were collected 6 weeks post-inoculation
707 with *R. irregularis* and cleared by boiling (95°C) in 10% KOH for 5 minutes, rinsed with water,
708 then stained by boiling in an acidic ink solution (5% acetic acid, 5% Sheaffer black ink #94321,
709 in water) to reveal fungal structures. Overall intraradical colonization rates and arbuscular
710 density were estimated in ink-stained roots under a stereomicroscope (Leica S6E) using the
711 gridline intersect method.

712

713 **Microscopy image analyses**

714 Analysis of confocal t-series was performed using the Fiji software[80]. Intensity data were
715 calculated from selected regions of interest (ROIs), corresponding to single nuclei, imaged in
716 independent roots, in 2-3 independent experiments. Maximal z-projections of stacks and
717 merged confocal images were prepared using Leica confocal software or Fiji. To quantify
718 relative amplitudes of Ca^{2+} spiking, the mean fluorescence of each ROI was measured as a
719 function of time and used to determine the Signal-to-Noise Ratio (SNR). The SNR measures
720 the difference between the fluorescence at each time-point (F_t) and the fluorescence baseline,
721 calculated as the average of 4 fluorescence values taken 10 and 15 sec before and after t (F_{t-}
722 $_3$; F_{t-2}; F_{t2+}; F_{t+3}). A threshold of 0.3 was applied to the SNR to define individual peaks, and the
723 amplitude of Ca^{2+} spiking was calculated for each nucleus as the mean peak SNR value. Spiking
724 frequency, defined as the number of peaks observed in 10 min, was also calculated.

725 Scanned images of β-galactosidase-stained nodules from R108* and *ann1-3* (10 dpi) were
726 imported to Ilastik software[81] to enable machine-learning recognition of blue β-galactosidase-
727 stained nodules (pixel-based classification method). Objects identified as nodules were
728 exported in a new single segmentation .tiff file for analysis in ImageJ to measure specific
729 nodule features (length, size and infection level, based on the blue intensity of rhizobial β-
730 galactosidase activity).

731

732 **Transient expression assays in *N. benthamiana* leaves**

733 An *A. tumefaciens* GV3101 strain carrying the *pMtAnn1:GUS* fusion construct (in pLP100) was
734 used for infiltration studies in *N. benthamiana* alone or with *A. tumefaciens* GV3103 strains
735 carrying *p35S:NIN* or *p35S:NINΔ* constructs[52], designed to constitutively express NIN or NINΔ
736 under the 35S promoter in transactivation experiments. Briefly, *A. tumefaciens* strains grown
737 overnight at 28°C in Luria-Bertani with appropriate antibiotics were harvested and
738 resuspended in Agromix (10 mM $MgCl_2$, 10 mM MES/KOH pH 5.6 and Acetosyringone in DMSO
739 Sigma-Aldrich 150 µM) and kept in the dark for at least 2h, at room temperature. Equal
740 volumes of *A. tumefaciens* cultures (OD_{600}=0.25) were used to co-infiltrate leaf discs of 3-week-
741 old *N. benthamiana* plants. Infiltrated plants were kept at 21°C in a growth chamber (16-h
742 photoperiod and a light intensity of 70 mE m22 s21) for 36 h prior to histochemical GUS assays
743 or storage at -70°C prior to protein extraction for Western-blot or fluorimetric GUS assays.

744

745 **Western blot analyses**

746 *N. benthamiana* leaf discs, previously stored at -80°C, were ground using a MM400 (Retsch)
747 crusher and resuspended in Laemmli 2X sample buffer for SDS-PAGE (Bio-rad). Samples were
748 then placed at 95°C for 3min and centrifuged at 13200 rpm for 1 min. For each sample, 10 µL
749 of the supernatant was loaded in a polyacrylamide 4-15% Mini-PROTEAN precast gel (Bio-Rad)
750 along with 5 µL of pre-stained protein ladder marker (ThermoScientific, Lithuania). The Mini-
751 Protean tank Electrophoresis System (Biorad, USA) was used for gel migration in 1 X
752 Tris/Glycine/SDS Buffer (Bio-Rad). Protein transfer to nitrocellulose membranes (Bio-Rad) was
753 performed using a Trans-Blot Turbo semi-dry transfer system (Bio-Rad). Membranes were
754 stained with Ponceau Red before incubation for 1 h in blocking 1 x TBS solution (Tris base, NaCl
755 and H_2O), 0.1 % Tween, 5 % milk at room temperature, with mild agitation, before rinsing 3 x
756 in TBS-Tween 0.1 % for 10 min, and incubated overnight in the same solution at 4°C with a
757 6000 X dilution of anti-HA-peroxidase antibodies (Sigma-Aldrich) in 0.5 % milk in TBS-Tween
758 0.1 % to reveal HA-tagged NIN proteins following chemiluminescence revelation using the
759 Clarity Western ECL Substrate (Bio-Rad) and the ChemiDoc Touch imaging system (Bio-Rad).

760

761 **Acetylene reduction assay**

762 To assess nitrogenase activity, grouped nodules were isolated from root systems of plants
763 grown in pots 3 weeks after inoculation with *Sm*2011-LacZ and tested for acetylene reduction.
764 Nodules were incubated at 25°C in sealed 60 mL vials containing 0.5 mL of nitrogen-free
765 Fahraeus liquid medium in the presence of 10 % (v/v) acetylene for 3 h. 400 µL of gaz was then
766 collected from each vial and ethylene production was quantified by gas chromatography
767 (model no. GC 7280A; Agilent Technologies, Lexington, MA).

768

769 **RNA extraction and quantitative RT-PCR analysis**

770 Total RNA was extracted from *M. truncatula* control and rhizobia-inoculated roots (4-5 dpi)
771 using the Macherey-Nagel total RNA isolation kit according to the manufacturer's instructions.
772 DNA-free RNA samples were quantified and RNA integrity was verified by Agilent RNA Nano
773 Chip (Agilent Technologies). First-strand complementary DNA synthesis was performed using
774 1 µg of total RNA using an anchored oligo (dT) and Transcriptor Reverse Transcriptase (Roche)
775 following the manufacturers' protocol. Quantitative RT-PCR was performed on 384-well
776 plates, with the Light Cycler 480 system (Roche) and using the SYBR Green I Master mix

(Roche), according to the manufacturer's instructions. Reactions and cycling conditions were performed as described before[29] using Primer pairs listed in Supplementary Table S1. The specificity of the PCR amplification was verified by analysing the PCR dissociation curve and sequencing of the PCR product. Transcript levels were normalized to the endogenous Ubiquitin reference.

Phylogenetic analysis

Protein sequence of *MtAnn1* (MtrunA17_Chr8g0352611) was used as query to search against a database containing 227 plant genomes covering the main lineages of green plants and five SAR genomes as outgroups using the BLASTp v2.14.0+ with an e-value threshold of 1e-10[55]. Homologous proteins were then aligned using Muscle v5.1 with the "super5" option[82] and trimmed to remove positions with more than 60% of gaps using trimAl v1.4.rev22[83]. The trimmed alignment served as matrix for phylogenetic reconstruction using FastTree v2.1.11-OpenMP[84]. To gain insights about the evolution of Ann1 in relation with the nitrogen-fixing symbiosis, the flowering clade corresponding containing orthologs of MtAnn1 has been extracted and proteins re-aligned using Muscle with default parameters before trimming as described above. Few spurious sequences with obvious mispositioning and abnormal short sequences were removed. Then, maximum likelihood tree has been reconstructed using IQ-TREE v2.1.2[85] after testing the best evolution model using ModelFinder[86] as implemented in IQ-TREE2 and according to the Bayesian Information Criteria. Branch supports have been tested with 10,000 replicates of both SH-aLRT[87] and UltraFast Bootstraps with UFBoot2[88]. Finally, trees were visualized and annotated in the iTOL platform v6.8.1[89].

Graph generation and Statistical Analyses

Graph preparation and statistical analyses were performed using R (http://r-project. org), with the exception of data in Fig. 6J, which was generated using Microsoft Excel and for which statistical contingency analysis was performed using GraphPad Prism 10. Normal distribution of the data was evaluated using the Shapiro-Wilk test, and homogeneity of variance was assessed using Fisher or Bartlett tests. Parametric statistical tests (t-test, ANOVA) were used to analyze data with a normal distribution, while the non-parametric Mann-Whitney statistical test was used for data with a non-normal distribution. When applicable, a transformation was performed to normalize data distribution (Log10 or BoxCox). Number of individually analyzed samples (n), replicates and *p* significance levels are indicated in Figure legends. In details, data were analyzed as follows: values in Fig. 2E follow a normal distribution and display homogeneous variance, so a two-tailed Student t-test was performed (t=-3.0927, df=39, p=0.0037). Values in Fig. 2F do not follow a normal distribution and were thus analyzed using a two-tailed Mann-Whitney test (W=315, p=0.1531). Log10-transformed values in Fig. 4E follow a normal distribution and variance homogeneity and were thus analyzed using one-way ANOVA followed by Tukey honest significant difference (HSD) tests (F=149.5, df=2, p<2e-16). Values in Fig. 5D follow a normal distribution and variance homogeneity and were thus analyzed using a two-tailed Student t-test (t=-3.51, df=89, p=0.0007). Values in Fig. 5E display a non-normal distribution and were thus analyzed using a two-tailed Mann-Whitney test (W=163255, p=1.26e-07). Log10-transformed values in Fig. 5F show a normal distribution and variance homogeneity, and were thus analyzed using a two-tailed Student t-test (t=-3.066,

821 df=27, p=0.0049). Values in Fig. 6A-C, do not follow a normal distribution, they were thus
822 analyzed using two-tailed Mann-Whitney tests (6A: W=1189.5, p=0.0487; 6B: W=1207.5,
823 p=0.0332; 6C: W=1233.5, p=0.0182). For Fig. 6J, a chi-square test was performed on a
824 contingency table reporting the number of cortically-extended ITs per individual NP for WT
825 and *ann1-3* plants (χ_2=15.35, df=2, p=0.0005). Values in Fig. 6K with a non-normal distribution
826 were analyzed using a two-tailed Mann-Whitney test (W=180905, p=2.2e-16). Values in Fig.
827 7A-B, which show a normal distribution and variance homogeneity were analyzed using one-
828 tailed Student t-tests, due to the low number of values (7A: t=2.1821, df=9, p=0.0285; 7B:
829 t=0.9612, df=22, p=0.1735). In Fig. 7C, values do not follow a normal distribution, thus a two-
830 tailed Mann-Whitney test was performed (W=9944, p=0.0018). In Fig. 8, values in 8A and
831 BoxCox-transformed values in 8B (λ=1.353535) show a normal distribution and homogeneity
832 of variance and were thus analyzed using two-tailed Student t-test (8A: t=3.6816, df=72,
833 p=0.0004448; 8B: t=3.8831, df=72, p=0.0002265). In Supplementary Fig. S1E-F, values show a
834 non-normal distribution and were thus analyzed using two-tailed Mann-Whitney tests (S1E:
835 W=853, p=1.811e-07; S1F: W=205, p=2.893e-05). In Supplementary Fig. S4B-C, BoxCox-
836 transformed S4B values (λ= 0.1010101) and Log10-transformed S4C values follow a normal
837 distribution and homogeneity of variance and were thus analyzed using one-way ANOVA
838 followed by Tukey honest significant difference (HSD) tests (S4B: F=681.2, df=4, p<2e-16 ; S4C:
839 F=2.4, df=3, p=0.0783). In Supplementary Fig. S6E-G, values follow a normal distribution and
840 variance homogeneity in S6E, hence a two-tailed Student t-test was carried out (t=2.4153,
841 df=99, p=0.0176), while values in S6F-G do not follow a normal distribution, thus two-tailed
842 Mann-Whitney tests were applied (S6F: W=1724, p=0.0023; S6G: W=1473.5, p=0.1759). In
843 Supplementary Fig. S7C-E, values do not follow a normal distribution in S7C and E and were
844 thus analyzed using two-tailed Mann-Whitney tests (S7C: W=18215, p=0.3726; S7E: W=86,
845 p=0.57), which values in S7D follow a normal distribution and variance homogeneity, so values
846 were analyzed using a two-tailed Student t-test (t=-1.0271, df=10, p=0.3286).

847

848 **Data availability**

849 The authors declare that all data supporting the results of this study are available within the
850 article and its Supplementary Information Files. Materials generated in this study are available
851 from the corresponding authors upon request.

852

853 ## References

854 1 Lanfranco, L., Fiorilli, V. & Gutjahr, C. Partner communication and role of nutrients in the
855 arbuscular mycorrhizal symbiosis. *New Phytol* **220**, 1031-1046 (2018).
856 https://doi.org/10.1111/nph.15230
857 2 Huisman, R. & Geurts, R. A Roadmap toward Engineered Nitrogen-Fixing Nodule Symbiosis.
858 *Plant Commun* **1**, 100019 (2020). https://doi.org/10.1016/j.xplc.2019.100019
859 3 Griesmann, M. *et al.* Phylogenomics reveals multiple losses of nitrogen-fixing root nodule
860 symbiosis. *Science* **361** (2018). https://doi.org/10.1126/science.aat1743
861 4 Libourel, C. *et al.* Comparative phylotranscriptomics reveals ancestral and derived root nodule
862 symbiosis programmes. *Nat Plants* **9**, 1067-1080 (2023). https://doi.org/10.1038/s41477-023-
863 01441-w
864 5 Charpentier, M. Calcium Signals in the Plant Nucleus: Origin and Function. *J Exp Bot* (2018).
865 https://doi.org/10.1093/jxb/ery160

866 6 Genre, A. & Russo, G. Does a Common Pathway Transduce Symbiotic Signals in Plant-Microbe
867 Interactions? *Front Plant Sci* **7**, 96 (2016). https://doi.org/10.3389/fpls.2016.00096
868 7 Krönauer, C. & Radutoiu, S. Understanding Nod factor signalling paves the way for targeted
869 engineering in legumes and non-legumes. *Curr Opin Plant Biol* **62**, 102026 (2021).
870 https://doi.org/10.1016/j.pbi.2021.102026
871 8 Lévy, J. *et al.* A putative Ca2+ and calmodulin-dependent protein kinase required for bacterial
872 and fungal symbioses. *Science* **303**, 1361-1364 (2004).
873 https://doi.org/10.1126/science.1093038
874 9 Tirichine, L. *et al.* Deregulation of a Ca2+/calmodulin-dependent kinase leads to spontaneous
875 nodule development. *Nature* **441**, 1153-1156 (2006). https://doi.org/10.1038/nature04862
876 10 Singh, S., Katzer, K., Lambert, J., Cerri, M. & Parniske, M. CYCLOPS, a DNA-binding
877 transcriptional activator, orchestrates symbiotic root nodule development. *Cell Host Microbe*
878 **15**, 139-152 (2014). https://doi.org/10.1016/j.chom.2014.01.011
879 11 Cerri, M. R. *et al.* The ERN 1 transcription factor gene is a target of the CC a MK/CYCLOPS
880 complex and controls rhizobial infection in Lotus japonicus. *New Phytologist* **215**, 323-337
881 (2017).
882 12 Pimprikar, P. & Gutjahr, C. Transcriptional Regulation of Arbuscular Mycorrhiza Development.
883 *Plant and Cell Physiology* **59**, 678-695 (2018). https://doi.org/10.1093/pcp/pcy024
884 13 De Carvalho-Niebel, F., Timmers, A. C., Chabaud, M., Defaux-Petras, A. & Barker, D. G. The Nod
885 factor-elicited annexin MtAnn1 is preferentially localised at the nuclear periphery in
886 symbiotically activated root tissues of Medicago truncatula. *Plant J* **32**, 343-352 (2002).
887 14 Manthey, K. *et al.* Transcriptome profiling in root nodules and arbuscular mycorrhiza identifies
888 a collection of novel genes induced during Medicago truncatula root endosymbioses. *Mol*
889 *Plant Microbe Interact* **17**, 1063-1077 (2004). https://doi.org/10.1094/MPMI.2004.17.10.1063
890 15 Davies, J. M. Annexin-Mediated Calcium Signalling in Plants. *Plants (Basel)* **3**, 128-140 (2014).
891 https://doi.org/10.3390/plants3010128
892 16 Kodavali, P. K. *et al.* Structural and functional characterization of annexin 1 from Medicago
893 truncatula. *Plant Physiol Biochem* **73**, 56-62 (2013).
894 https://doi.org/10.1016/j.plaphy.2013.08.010
895 17 Malabarba, J. *et al.* ANNEXIN1 mediates calcium-dependent systemic defense in Arabidopsis
896 plants upon herbivory and wounding. *New Phytol* **231**, 243-254 (2021).
897 https://doi.org/10.1111/nph.17277
898 18 Liao, C., Zheng, Y. & Guo, Y. MYB30 transcription factor regulates oxidative and heat stress
899 responses through ANNEXIN-mediated cytosolic calcium signaling in Arabidopsis. *New Phytol*
900 **216**, 163-177 (2017). https://doi.org/10.1111/nph.14679
901 19 Richards, S. L. *et al.* Annexin 1 regulates the H2O2-induced calcium signature in Arabidopsis
902 thaliana roots. *Plant J* **77**, 136-145 (2014). https://doi.org/10.1111/tpj.12372
903 20 Gutjahr, C. & Parniske, M. Cell and developmental biology of arbuscular mycorrhiza symbiosis.
904 *Annu Rev Cell Dev Biol* **29**, 593-617 (2013). https://doi.org/10.1146/annurev-cellbio-101512-
905 122413
906 21 Gage, D. J. Infection and invasion of roots by symbiotic, nitrogen-fixing rhizobia during
907 nodulation of temperate legumes. *Microbiol Mol Biol Rev* **68**, 280-300 (2004).
908 https://doi.org/10.1128/MMBR.68.2.280-300.2004
909 22 Roth, R. *et al.* Arbuscular cell invasion coincides with extracellular vesicles and membrane
910 tubules. *Nat Plants* **5**, 204-211 (2019). https://doi.org/10.1038/s41477-019-0365-4
911 23 Ivanov, S., Austin, J., Berg, R. H. & Harrison, M. J. Extensive membrane systems at the host-
912 arbuscular mycorrhizal fungus interface. *Nat Plants* **5**, 194-203 (2019).
913 https://doi.org/10.1038/s41477-019-0364-5
914 24 Fournier, J. *et al.* Remodeling of the infection chamber before infection thread formation
915 reveals a two-step mechanism for rhizobial entry into the host legume root hair. *Plant*
916 *physiology* **167**, 1233--1242 (2015). https://doi.org/10.1104/pp.114.253302

917 25 Liang, P. *et al.* Formin-mediated bridging of cell wall, plasma membrane, and cytoskeleton in
918 symbiotic infections of Medicago truncatula. *Curr Biol* **31**, 2712-2719.e2715 (2021).
919 https://doi.org/10.1016/j.cub.2021.04.002
920 26 Su, C. *et al.* Transcellular progression of infection threads in Medicago truncatula roots is
921 associated with locally confined cell wall modifications. *Curr Biol* **33**, 533-542.e535 (2023).
922 https://doi.org/10.1016/j.cub.2022.12.051
923 27 Liu, C. W. *et al.* A protein complex required for polar growth of rhizobial infection threads. *Nat*
924 *Commun* **10**, 2848 (2019). https://doi.org/10.1038/s41467-019-10029-y
925 28 Lace, B. *et al.* RPG acts as a central determinant for infectosome formation and cellular
926 polarization during intracellular rhizobial infections. *Elife* **12** (2023).
927 https://doi.org/10.7554/eLife.80741
928 29 Gaudioso-Pedraza, R. *et al.* Callose-Regulated Symplastic Communication Coordinates
929 Symbiotic Root Nodule Development. *Curr Biol* **28**, 3562-3577.e3566 (2018).
930 https://doi.org/10.1016/j.cub.2018.09.031
931 30 Xiao, T. T. *et al.* Fate map of Medicago truncatula root nodules. *Development* **141**, 3517-3528
932 (2014). https://doi.org/10.1242/dev.110775
933 31 Lin, J., Frank, M. & Reid, D. No Home without Hormones: How Plant Hormones Control Legume
934 Nodule Organogenesis. *Plant Commun* **1**, 100104 (2020).
935 https://doi.org/10.1016/j.xplc.2020.100104
936 32 Chaulagain, D. & Frugoli, J. The Regulation of Nodule Number in Legumes Is a Balance of Three
937 Signal Transduction Pathways. *Int J Mol Sci* **22** (2021). https://doi.org/10.3390/ijms22031117
938 33 Genre, A., Chabaud, M., Faccio, A., Barker, D. G. & Bonfante, P. Prepenetration apparatus
939 assembly precedes and predicts the colonization patterns of arbuscular mycorrhizal fungi
940 within the root cortex of both Medicago truncatula and Daucus carota. *Plant Cell* **20**, 1407-
941 1420 (2008). https://doi.org/10.1105/tpc.108.059014
942 34 Van Brussel, A. A. N. *et al*. Induction of pre-infection thread structures in the leguminous host
943 plant by mitogenic lipo-oligosaccharides of Rhizobium. *Science* **257**, 70-72 (1992).
944 35 Genre, A., Ortu, G., Bertoldo, C., Martino, E. & Bonfante, P. Biotic and abiotic stimulation of
945 root epidermal cells reveals common and specific responses to arbuscular mycorrhizal fungi.
946 *Plant Physiol* **149**, 1424-1434 (2009). https://doi.org/10.1104/pp.108.132225
947 36 Russo, G. & Genre, A. Divide and Be Conquered-Cell Cycle Reactivation in Arbuscular
948 Mycorrhizal Symbiosis. *Front Plant Sci* **12**, 753265 (2021).
949 https://doi.org/10.3389/fpls.2021.753265
950 37 Batzenschlager, M., Lace, B., Zhang N, Su, C., Egli, S., Krohn, P., Salfeld, J., D. F. A., Laux, T., Ott,
951 T. Competence for transcellular infection in the root cortex involves a post-replicative, cell-
952 cycle exit decision in Medicago truncatula. bioRxiv (2023).
953 38 Perrine-Walker, F. M., Lartaud, M., Kouchi, H. & Ridge, R. W. Microtubule array formation
954 during root hair infection thread initiation and elongation in the Mesorhizobium-Lotus
955 symbiosis. *Protoplasma* **251**, 1099-1111 (2014). https://doi.org/10.1007/s00709-014-0618-z
956 39 Yang, W. C. *et al.* Rhizobium nod factors reactivate the cell cycle during infection and nodule
957 primordium formation, but the cycle is only completed in primordium formation. *Plant Cell* **6**,
958 1415-1426 (1994). https://doi.org/10.1105/tpc.6.10.1415
959 40 Timmers, A. C., Auriac, M. C. & Truchet, G. Refined analysis of early symbiotic steps of the
960 Rhizobium-Medicago interaction in relationship with microtubular cytoskeleton
961 rearrangements. *Development* **126**, 3617-3628 (1999).
962 41 Fournier, J. *et al.* Mechanism of infection thread elongation in root hairs of Medicago
963 truncatula and dynamic interplay with associated rhizobial colonization. *Plant Physiol* **148**,
964 1985-1995 (2008). https://doi.org/10.1104/pp.108.125674
965 42 Sieberer, B. J., Chabaud, M., Fournier, J., Timmers, A. C. & Barker, D. G. A switch in Ca2+ spiking
966 signature is concomitant with endosymbiotic microbe entry into cortical root cells of Medicago
967 truncatula. *Plant J* **69**, 822-830 (2012). https://doi.org/10.1111/j.1365-313X.2011.04834.x

43 Takeda, N., Maekawa, T. & Hayashi, M. Nuclear-localized and deregulated calcium- and calmodulin-dependent protein kinase activates rhizobial and mycorrhizal responses in Lotus japonicus. *Plant Cell* **24**, 810-822 (2012). https://doi.org/10.1105/tpc.111.091827

44 Kelner, A., Leitão, N., Chabaud, M., Charpentier, M. & de Carvalho-Niebel, F. Dual Color Sensors for Simultaneous Analysis of Calcium Signal Dynamics in the Nuclear and Cytoplasmic Compartments of Plant Cells. *Front Plant Sci* **9**, 245 (2018). https://doi.org/10.3389/fpls.2018.00245

45 Schnabel, E., Journet, E. P., de Carvalho-Niebel, F., Duc, G. & Frugoli, J. The Medicago truncatula SUNN gene encodes a CLV1-like leucine-rich repeat receptor kinase that regulates nodule number and root length. *Plant Mol Biol* **58**, 809-822 (2005). https://doi.org/10.1007/s11103-005-8102-y

46 Cerri, M. R. *et al.* Medicago truncatula ERN transcription factors: regulatory interplay with NSP1/NSP2 GRAS factors and expression dynamics throughout rhizobial infection. *Plant Physiol* **160**, 2155-2172 (2012). https://doi.org/10.1104/pp.112.203190

47 Middleton, P. H. *et al.* An ERF transcription factor in Medicago truncatula that is essential for Nod factor signal transduction. *Plant Cell* **19**, 1221-1234 (2007). https://doi.org/10.1105/tpc.106.048264

48 Cerri, M. R. *et al.* The Symbiosis-Related ERN Transcription Factors Act in Concert to Coordinate Rhizobial Host Root Infection. *Plant Physiol* **171**, 1037-1054 (2016). https://doi.org/10.1104/pp.16.00230

49 Wais, R. J. *et al.* Genetic analysis of calcium spiking responses in nodulation mutants of Medicago truncatula. *Proc Natl Acad Sci U S A* **97**, 13407-13412 (2000). https://doi.org/10.1073/pnas.230439797

50 Rival, P. *et al.* Epidermal and cortical roles of NFP and DMI3 in coordinating early steps of nodulation in Medicago truncatula. *Development* **139**, 3383-3391 (2012). https://doi.org/10.1242/dev.081620

51 Schiessl, K. *et al.* NODULE INCEPTION Recruits the Lateral Root Developmental Program for Symbiotic Nodule Organogenesis in Medicago truncatula. *Curr Biol* **29**, 3657-3668.e3655 (2019). https://doi.org/10.1016/j.cub.2019.09.005

52 Vernie, T. *et al.* The NIN Transcription Factor Coordinates Diverse Nodulation Programs in Different Tissues of the Medicago truncatula Root. *Plant Cell* **27**, 3410-3424 (2015). https://doi.org/10.1105/tpc.15.00461

53 Liu, H. *et al.* A genetic screen for plant mutants with altered nodulation phenotypes in response to rhizobial glycan mutants. *New Phytol* **220**, 526-538 (2018). https://doi.org/10.1111/nph.15293

54 Vasse, J., de Billy, F., Camut, S. & Truchet, G. Correlation between ultrastructural differentiation of bacteroids and nitrogen fixation in alfalfa nodules. *J Bacteriol* **172**, 4295-4306 (1990). https://doi.org/10.1128/jb.172.8.4295-4306.1990

55 Radhakrishnan, G. V. *et al.* An ancestral signalling pathway is conserved in intracellular symbioses-forming plant lineages. *Nat Plants* **6**, 280-289 (2020). https://doi.org/10.1038/s41477-020-0613-7

56 Clark, G. B., Morgan, R. O., Fernandez, M. P. & Roux, S. J. Evolutionary adaptation of plant annexins has diversified their molecular structures, interactions and functional roles. *New Phytol* **196**, 695-712 (2012). https://doi.org/10.1111/j.1469-8137.2012.04308.x

57 Seguí-Simarro, J. M., Coronado, M. J. & Staehelin, L. A. The mitochondrial cycle of Arabidopsis shoot apical meristem and leaf primordium meristematic cells is defined by a perinuclear tentaculate/cage-like mitochondrion. *Plant Physiol* **148**, 1380-1393 (2008). https://doi.org/10.1104/pp.108.126953

58 Costa, A., Navazio, L. & Szabo, I. The contribution of organelles to plant intracellular Calcium signalling. *J Exp Bot* (2018). https://doi.org/10.1093/jxb/ery185

59 Cui, Y. *et al.* A whole-cell electron tomography model of vacuole biogenesis in Arabidopsis root cells. *Nat Plants* **5**, 95-105 (2019). https://doi.org/10.1038/s41477-018-0328-1

1020 60 Genre, A. *et al.* Multiple exocytotic markers accumulate at the sites of perifungal membrane
1021 biogenesis in arbuscular mycorrhizas. *Plant Cell Physiol* **53**, 244-255 (2012).
1022 https://doi.org/10.1093/pcp/pcr170
1023 61 Viotti, C. ER and vacuoles: never been closer. *Front Plant Sci* **5**, 20 (2014).
1024 https://doi.org/10.3389/fpls.2014.00020
1025 62 Evans, R. C. & Blackwell, K. T. Calcium: amplitude, duration, or location? *Biol Bull* **228**, 75-83
1026 (2015). https://doi.org/10.1086/BBLv228n1p75
1027 63 Whalley, H. J. & Knight, M. R. Calcium signatures are decoded by plants to give specific gene
1028 responses. *New Phytol* **197**, 690-693 (2013). https://doi.org/10.1111/nph.12087
1029 64 Xu, T., Niu, J. & Jiang, Z. Sensing Mechanisms: Calcium Signaling Mediated Abiotic Stress in
1030 Plants. *Front Plant Sci* **13**, 925863 (2022). https://doi.org/10.3389/fpls.2022.925863
1031 65 Del Cerro, P. *et al.* Engineered CaM2 modulates nuclear calcium oscillation and enhances
1032 legume root nodule symbiosis. *Proc Natl Acad Sci U S A* **119**, e2200099119 (2022).
1033 https://doi.org/10.1073/pnas.2200099119
1034 66 Laohavisit, A. *et al.* Arabidopsis annexin1 mediates the radical-activated plasma membrane
1035 Ca^{2}+- and K+-permeable conductance in root cells. *Plant Cell* **24**, 1522-1533 (2012).
1036 https://doi.org/10.1105/tpc.112.097881
1037 67 Tichá, M. *et al.* Advanced Microscopy Reveals Complex Developmental and Subcellular
1038 Localization Patterns of ANNEXIN 1 in. *Front Plant Sci* **11**, 1153 (2020).
1039 https://doi.org/10.3389/fpls.2020.01153
1040 68 Zhao, Z. X. *et al.* ANNEXIN 8 negatively regulates RPW8.1-mediated cell death and disease
1041 resistance in Arabidopsis. *J Integr Plant Biol* **63**, 378-392 (2021).
1042 https://doi.org/10.1111/jipb.13025
1043 69 Vais, H. *et al.* ER-luminal [Ca2+] regulation of InsP3 receptor gating mediated by an ER-luminal
1044 peripheral Ca2+-binding protein. *Elife* **9** (2020). https://doi.org/10.7554/eLife.53531
1045 70 Peiter, E. The plant vacuole: emitter and receiver of calcium signals. *Cell Calcium* **50**, 120-128
1046 (2011). https://doi.org/10.1016/j.ceca.2011.02.002
1047 71 Himschoot, E., Pleskot, R., Van Damme, D. & Vanneste, S. The ins and outs of Ca. *Curr Opin*
1048 *Plant Biol* **40**, 131-137 (2017). https://doi.org/10.1016/j.pbi.2017.09.003
1049 72 Ruan, H., Wang, T., Ren, H. & Zhang, Y. AtFH5-labeled secretory vesicles-dependent calcium
1050 oscillation drives exocytosis and stepwise bulge during pollen germination. *Cell Rep* **42**, 113319
1051 (2023). https://doi.org/10.1016/j.celrep.2023.113319
1052 73 Konopka-Postupolska, D. & Clark, G. Annexins as Overlooked Regulators of Membrane
1053 Trafficking in Plant Cells. *Int J Mol Sci* **18** (2017). https://doi.org/10.3390/ijms18040863
1054 74 Takatsuka, H., Higaki, T. & Ito, M. At the Nexus between Cytoskeleton and Vacuole: How Plant
1055 Cytoskeletons Govern the Dynamics of Large Vacuoles. *Int J Mol Sci* **24** (2023).
1056 https://doi.org/10.3390/ijms24044143
1057 75 Lhuissier, F. G. P., De Ruijter, N. C. A., Sieberer, B. J., Esseling, J. J., Emons, A. M. C. Time Course
1058 of Cell Biological Events Evoked in Legume Root Hairs by Rhizobium Nod Factors: State of the
1059 Art. *Annals of Botany* **87**, 289-302 (2001).
1060 76 Sieberer, B. a. E., Anne Mie C. Cytoarchitecture and pattern of cytoplasmic streaming in root
1061 hairs of Medicago truncatula during development and deformation by nodulation factors.
1062 *Protoplasma* **214**, 118-127 (2000).
1063 77 Carrasco-Castilla, J., Ortega-Ortega, Y., Jáuregui-Zúñiga, D., Juárez-Verdayes, M. A., Arthikala,
1064 M.-K., Monroy-Morales, E., Nava, N., Santana, O., Sánchez-López, R., Quinto, C. *Environmental*
1065 *and Experimental Botany* **153**, 108-119 (2018).
1066 78 Marsh, J. F. *et al.* Medicago truncatula NIN is essential for rhizobial-independent nodule
1067 organogenesis induced by autoactive calcium/calmodulin-dependent protein kinase. *Plant*
1068 *Physiol* **144**, 324-335 (2007). https://doi.org/10.1104/pp.106.093021
1069 79 Zeng, T. *et al.* Host- and stage-dependent secretome of the arbuscular mycorrhizal fungus
1070 Rhizophagus irregularis. *Plant J* **94**, 411-425 (2018). https://doi.org/10.1111/tpj.13908

80 Schindelin, J. *et al.* Fiji: an open-source platform for biological-image analysis. *Nat Methods* **9**, 676-682 (2012). https://doi.org/10.1038/nmeth.2019

81 Berg, S. *et al.* ilastik: interactive machine learning for (bio)image analysis. *Nat Methods* **16**, 1226-1232 (2019). https://doi.org/10.1038/s41592-019-0582-9

82 Edgar, R. C. Muscle5: High-accuracy alignment ensembles enable unbiased assessments of sequence homology and phylogeny. *Nat Commun* **13**, 6968 (2022). https://doi.org/10.1038/s41467-022-34630-w

83 Capella-Gutiérrez, S., Silla-Martínez, J. M. & Gabaldón, T. trimAl: a tool for automated alignment trimming in large-scale phylogenetic analyses. *Bioinformatics* **25**, 1972-1973 (2009). https://doi.org/10.1093/bioinformatics/btp348

84 Price, M. N., Dehal, P. S. & Arkin, A. P. FastTree 2--approximately maximum-likelihood trees for large alignments. *PLoS One* **5**, e9490 (2010). https://doi.org/10.1371/journal.pone.0009490

85 Minh, B. Q. *et al.* IQ-TREE 2: New Models and Efficient Methods for Phylogenetic Inference in the Genomic Era. *Mol Biol Evol* **37**, 1530-1534 (2020). https://doi.org/10.1093/molbev/msaa015

86 Kalyaanamoorthy, S., Minh, B. Q., Wong, T. K. F., von Haeseler, A. & Jermiin, L. S. ModelFinder: fast model selection for accurate phylogenetic estimates. *Nat Methods* **14**, 587-589 (2017). https://doi.org/10.1038/nmeth.4285

87 Guindon, S. *et al.* New algorithms and methods to estimate maximum-likelihood phylogenies: assessing the performance of PhyML 3.0. *Syst Biol* **59**, 307-321 (2010). https://doi.org/10.1093/sysbio/syq010

88 Hoang, D. T., Chernomor, O., von Haeseler, A., Minh, B. Q. & Vinh, L. S. UFBoot2: Improving the Ultrafast Bootstrap Approximation. *Mol Biol Evol* **35**, 518-522 (2018). https://doi.org/10.1093/molbev/msx281

89 Letunic, I. & Bork, P. Interactive Tree Of Life (iTOL) v5: an online tool for phylogenetic tree display and annotation. *Nucleic Acids Res* **49**, W293-W296 (2021). https://doi.org/10.1093/nar/gkab301

Acknowledgements

We thank Celine Remblière for providing seeds of the *M. truncatula dmi3* line carrying the *pEXT:DMI3* construct. The *M. truncatula* R108 mutant plants utilized in this research project, which are jointly owned by the Centre National De La Recherche Scientifique, were obtained from Noble Research Institute, LLC and were created through research funded, in part, by grants from the National Science Foundation, NSF #DBI-0703285 and NSF #IOS-1127155. This work was supported by French National Research grants TULIP ANR-10-LABX-41, COME-IN ANR-14-CE35-0007-01 and LIVE-SWITCH ANR-19-CE20-0026-01 to FdCN and by the European Research Council (ERC) under the European Union's Horizon 2020 research and innovation program (grant No. 759731) to CG. This work also benefited from specific financial assistance from the INRAE Plant Health and Environment department (SPE). A. G. was funded by an ANR postdoctoral grant (ANR-19-CE20-0026-01), A. K. and A. D. were funded by PhD grants from the French Ministry of National Education and Research. We acknowledge the TRI-FRAIB imaging facility, member of the national infrastructure France-BioImaging supported by the French National Research Agency (ANR-10-INBS-04).

Author contributions

Rhizobial symbiosis-related experiments were designed and performed by FdCN's team members: ultrastructural microscopy (MCA), live cell imaging in various genotypes (JF, AK, AG), promoter-GUS and Q-RT-PCR studies (LF), mutant/RNAi phenotyping (AG, AD). AM symbiosis-related experiments were designed and carried out by KH (promoter-GUS) and AG and NFF (mutant analysis). AG and AL set up the machine-learning nodule phenotyping ImageJ method, JK and PMD carried out the phylogenetic studies. AG, JF, AK, MCA, LF, KH, AD, NFF and JK analysed the data with contributions from PMD, CG or FdCN. FdCN designed the research and wrote the article with AG and JF and key contributions from the other authors.

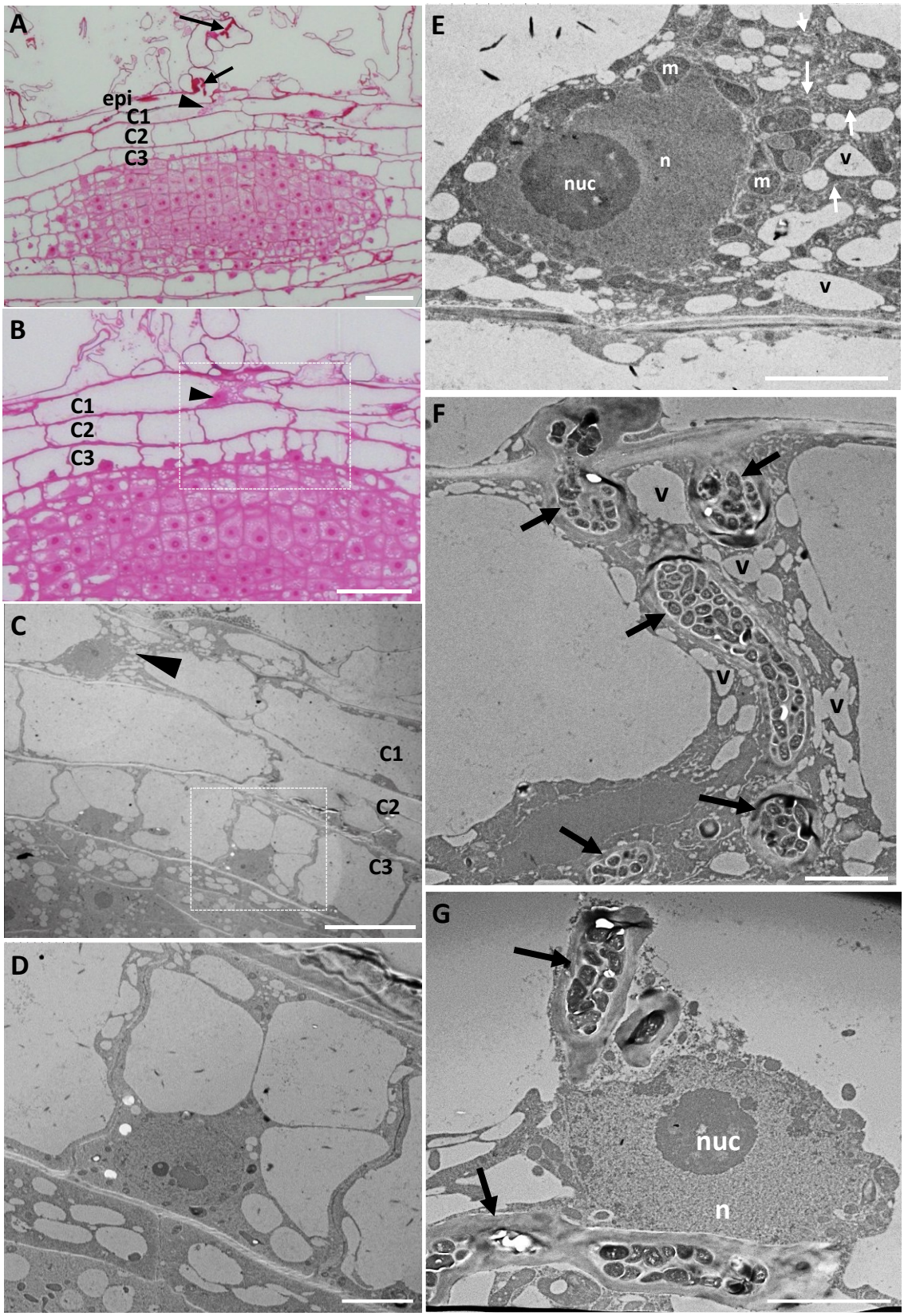

Fig. 1. Cell-specific structural changes in *M. truncatula* cells primed for infection.

(**A**-**B**) Representative images of longitudinal sections of *M. truncatula* roots 5 days after spot-inoculation with *S. meliloti.* These are consecutive 1 µm sections stained with basic fuchsin to reveal cell outlines and content. Arrows indicate ITs in root hair epidermal cells and

1131 arrowheads indicate a C1 cortical cell exhibiting pre-infection priming. The region of interest
1132 in **B** (highlighted by a white square) is visualised in **C**-**E** by transmission electron microscopy of
1133 80 nm sections. Note that the primed C1 outer cortical cell (arrowhead in **C**, and enlarged
1134 image in **E**) exhibits a unique structural organization compared with neighbouring cells. Primed
1135 cells comprise a cytoplasmic bridge enriched in endoplasmic reticulum (white arrows in **E**), and
1136 numerous vesicles or small vacuole-like (SV-like) structures (SVs) (v). They also have a large
1137 nucleus (n) surrounded by numerous mitochondria (m), a unique configuration not seen in
1138 other cells (for comparison, see C3 cells in **D** that will form the meristem). (**F**-**G**) At a later stage,
1139 when the IT (arrows) has progressed across the cytoplasmic bridge towards inner tissues, the
1140 nucleus is frequently found closely associated to the IT (**G**). Other abbreviations: nucleolus
1141 (nuc). Scale bars: **A**-**B** = 50 µm, **C** = 20 µm, **D**-**G** = 5 µm.

1142

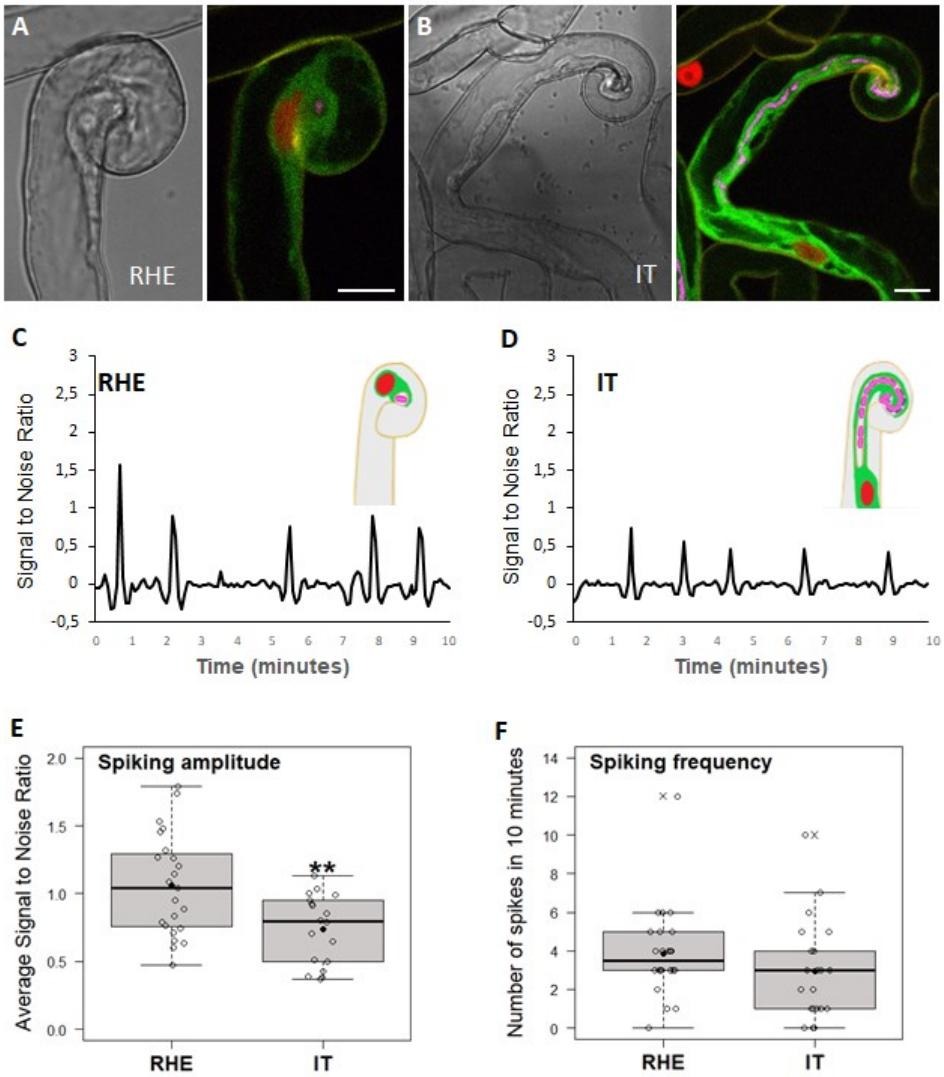

Fig. 2. Ca^{2+} spiking amplitude drops along root hair IT development.

(**A**-**B**) Representative bright-field and corresponding confocal images of (**A**) a root hair with entrapped CFP expressing (magenta)-*S. meliloti* (RHE) and (**B**) a root hair with a growing infection thread (IT) in *sunn-2*. Nuclei expressing the NR-GECO1 Ca^{2+} sensor appear in red, and the MtAnn1-GFP fluorescence (green) labels the cytoplasmic zone around the IT and the cytoplasmic bridge connecting and surrounding the nucleus. Scale bars: **A**-**B** = 10 µm. (**C**-**D**) Representative Ca^{2+} spiking traces of RHE (**C**) and growing IT stages (**D**). The relative concentration of Ca^{2+} ions in the nucleus is reflected by the intensity of NR-GECO1 fluorescence, expressed as signal-to-noise ratio (SNR, cf. Methods section). (**E**-**F**) Quantification of nuclear Ca^{2+} spiking: Spiking amplitude (**E**), expressed as average SNR of spikes per nucleus, and spiking frequency (**F**), expressed as number of spikes in 10 minutes per nucleus. Box plots represent the distribution of individual values (indicated by open circles) from root hairs with entrapped rhizobia (RHE, n=23 in **A** and n=24 in **F**) or with an IT (n=18 in **E** and n=21 in **F**) in *sunn2* 2-4 dpi with *S. meliloti* from three independent biological experiments. Median (central line), mean (solid black circle) and outliers (cross) are indicated. Two-tailed T-test (**E**) and Mann-Whitney test (**F**) of values were performed in R (asterisks indicate statistical difference; **$p < 0.01$). See also Figure S1 for Ca^{2+} spiking responses in *S. meliloti*-responsive root hairs of the nodulation-susceptible root zone in A17.

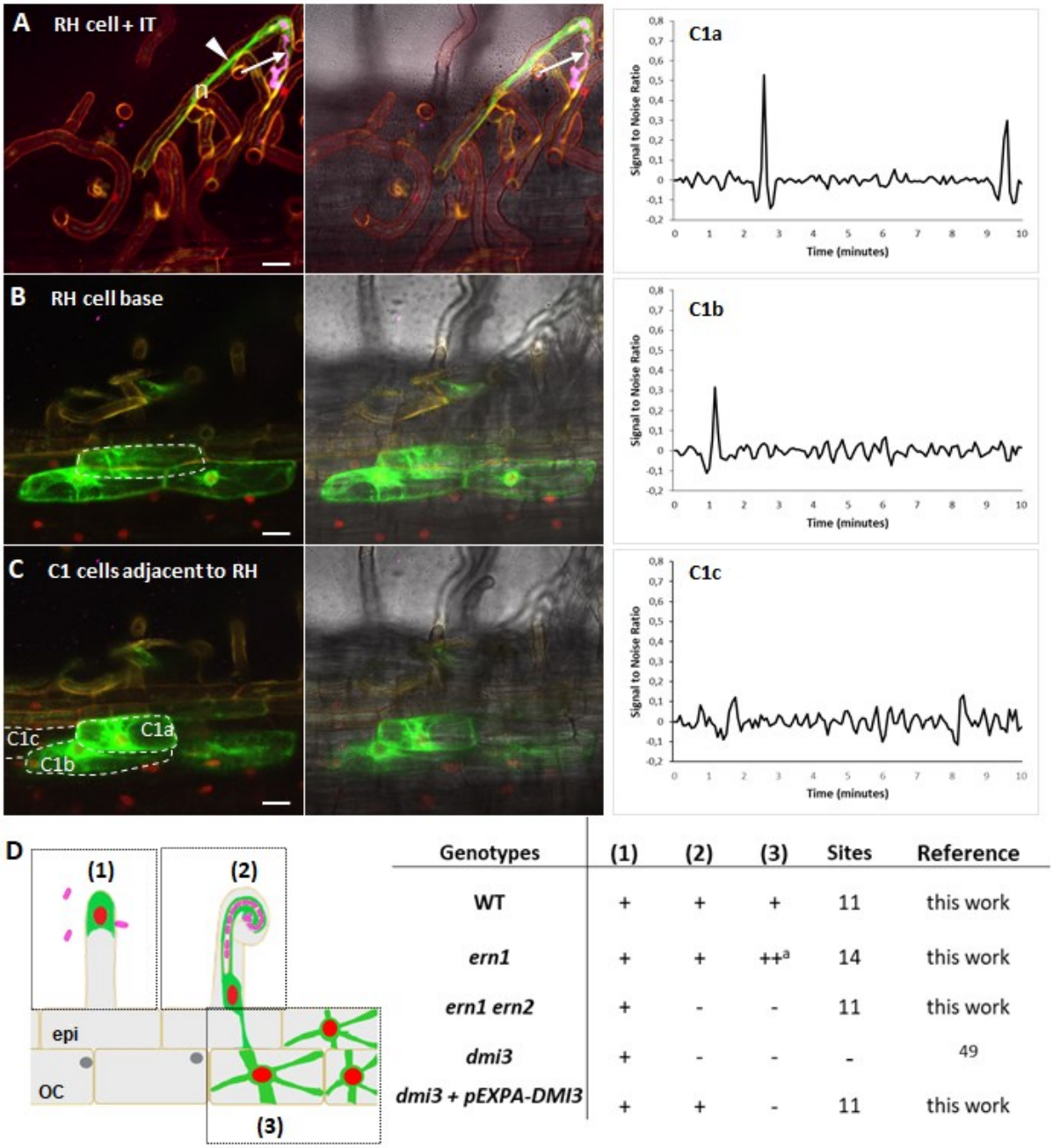

Genotypes	(1)	(2)	(3)	Sites	Reference
WT	+	+	+	11	this work
ern1	+	+	++[a]	14	this work
ern1 ern2	+	-	-	11	this work
dmi3	+	-	-	-	49
dmi3 + pEXPA-DMI3	+	+	-	11	this work

Fig. 3. Strong MtAnn1-GFP fusion fluorescence and low frequency Ca^{2+} spikes are hallmarks of pre-infection priming in the cortex.

Representative images of a root hair cell and neighbour outer cortex cells at a rhizobia infection site, in a root expressing MtAnn1-GFP (green) and NR-GECO1 (red). Confocal images from **A** to **C** illustrate the infected root hair with CFP-labelled rhizobia in IT (in magenta, arrow) and the nucleus (n) in front, guiding the growth of the IT in a cytoplasmic bridge (arrowhead) (**A**), the base of the RH cell (**B**, dotted line) and the neighbour C1a-c outer cortical cells (**C**, dotted lines). Images were obtained from A17 roots 4 dpi with *S. meliloti*. Representative traces of Ca^{2+} spiking from C1a, adjacent to the infected root hair, and neighbouring C1b and C1c cells. Note that only cortical cells co-expressing MtAnn1-GFP show detectable low frequency Ca^{2+} spiking (compare C1a-b and C1c). Traces are expressed as signal-to-noise ratio (SNR). (**D**) Genetic

1175 dissection of pre-infection priming responses by co-expression of MtAnn1-GFP and NR-GECO1
1176 in WT (A17 control) and in rhizobia-infection defective mutants (*ern1*, *ern1ern2*, *dmi3*). Left,
1177 schematic representation of Ca^{2+} spiking in *S. meliloti*-responsive non-infected root hairs of
1178 the nodulation-susceptible root zone (**1**), MtAnn1-GFP + Ca^{2+} spiking responses in infected
1179 root hairs (**2**) and infection primed cells in neighbouring epidermis or outer cortical cells (**3**) of
1180 the A17 WT control. Rhizobia are represented in pink, MtAnn1-GFP cytoplasmic labelling in
1181 green and nuclear Ca^{2+} spiking in red. Right, these responses are observed (+) or not (-) in
1182 different mutant backgrounds. All responses are observed in *ern1*, though deregulated (a) as
1183 indicated. Scale bars: **A**-**C** = 20 µm. See also Figures S1-S2.

1184

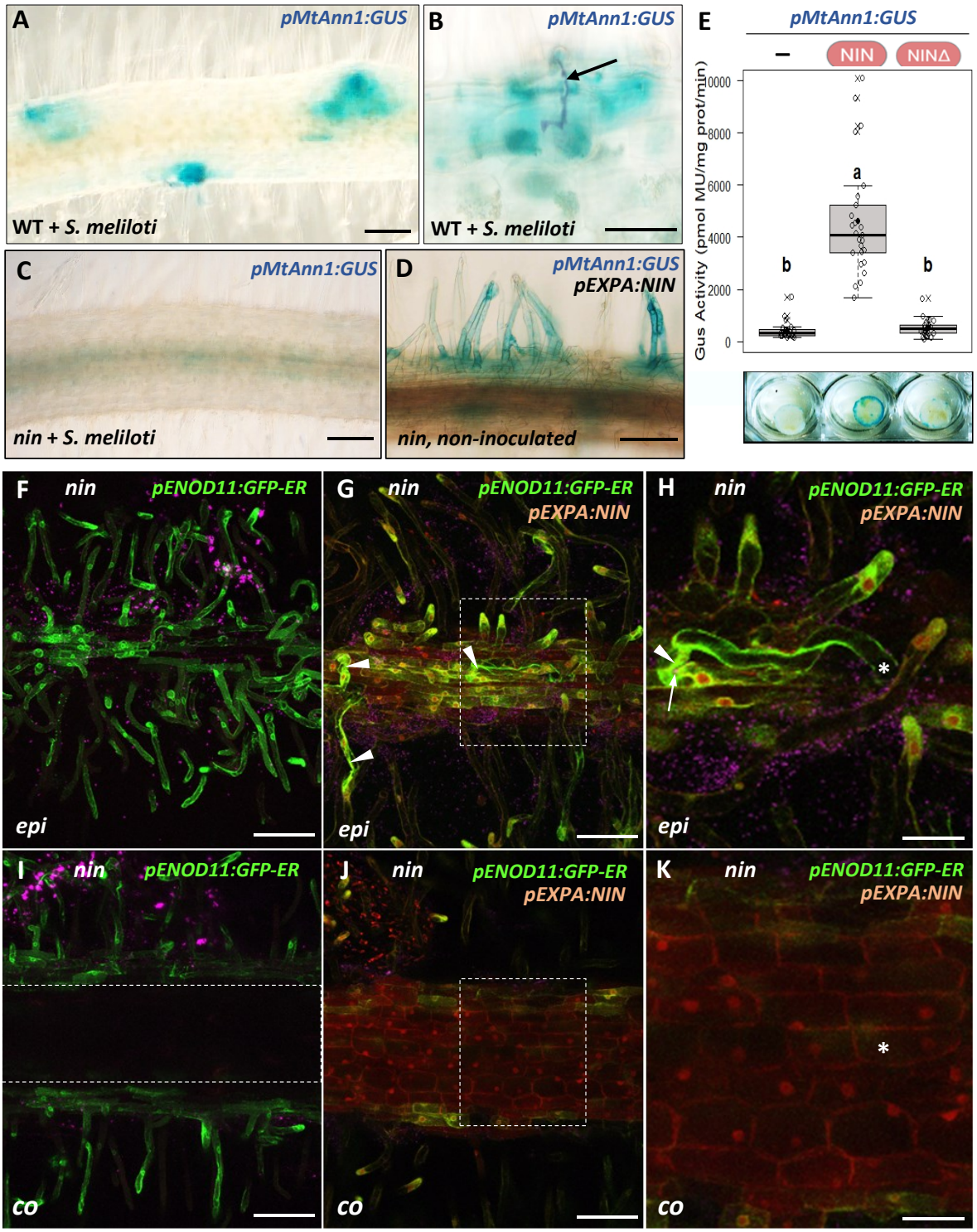

Fig. 4. NIN regulates cytoplasmic pre-infection priming and *MtAnn1* expression.

(**A**-**E**) Expression of the *pMtAnn1:GUS* fusion at infection sites in control WT (A17) roots at 4 dpi with *S. meliloti* (**A**-**B**). *LacZ*-expressing rhizobia are indicated in magenta (arrow) in **B**. This infection-related profile is abolished in *nin* (**C**). The expression of NIN under *pEXPA* induces the expression of the *pMtAnn1:GUS* fusion in the epidermis in the absence of rhizobia (**D**). Data in **A**-**D** are from two independent experiments (n=41 in A17, n=31 in *nin*, n=37 in *nin* + *pEXPA:NIN*). (**E**) Transactivation of the *pMtAnn1:GUS* fusion by NIN in *A. tumefaciens*-infiltrated leaf discs. Fluorimetric GUS assays were performed using 1 µg of total protein

extracts. Box plots represent the distribution of values (indicated as open circles) of individual plants (n=25 per sample) from 4 independent experiments. Median (central line), mean (solid black circle) and outliers (cross) are indicated. Different letters above the box blots indicate statistically significant difference (One-way ANOVA, α= 5%). Images of representative leaf discs are included. (**F**-**K**) *pENOD11:*GFP-ER expression in *nin* with or without epidermal-specific complementation with the *pEXPA:NIN* construct. Complemented roots (in **G**-**H**-**J**-**K**) co-express the *pUbiquitin*-driven fluorescent marker Ds-Red, which labels the cytosol and nucleoplasm in red. GFP-ER green fluorescence labels the perinuclear ER network, the tip of growing root hairs and the cytoplasmic column of primed root hair cells. In *nin* (**F**), GFP-ER labelling is only detected in perinuclear and root hair tip regions while in *nin* complemented with *pEXPA-NIN*, GFP-ER also labels cytoplasmic columns (arrowheads, **G** and **H**) in infection chamber-forming RHs (arrow in **H**). Adjacent OC1 cells show no green fluorescence in the cortex (see the boxed area in **I**) nor cytoplasmic reorganization (Ds-Red in **J**-**K**). **H** and **K** are boxed areas of **G** and **J**, respectively. Data were obtained from 2 independent experiments (n=19 for *nin* and n=19 for *nin* + *pEXPA:NIN*). Asterisks in **H** and **K** mark the xy position of the infected root hair base. Abbreviations: epi=epidermis; co=cortex. Scale bars: **A**, **C**, **D** = 100 µm, **B** = 50 µm, **F**, **G**, **I**, **J** = 100µm, **H**-**K** = 40 µm.

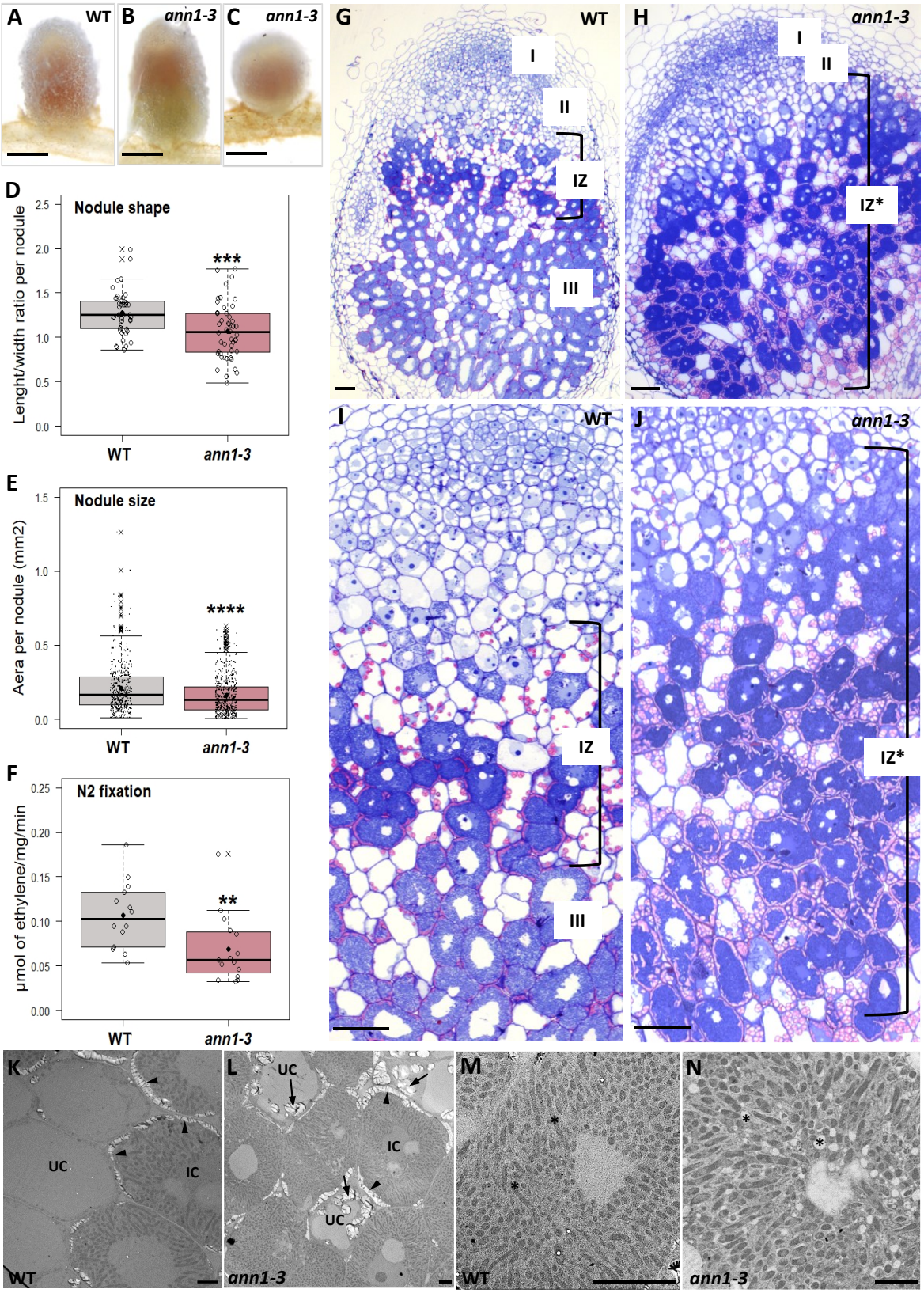

1212

1213 **Fig. 5. *MtAnn1* mutants show impaired nodule differentiation and function.**

1214 (**A**-**C**) Representative images of mature nodules developed in WT (**A**) and *ann1-3* mutant (**B**-**C**)
1215 roots 21 dpi with *S. meliloti*. (**D**) Nodule shape, represented by the ratio of maximal length to
1216 maximal width of individual nodules, was measured on WT (n=43) and *ann1-3* (n=48) mutant

nodules from 3 independent experiments. (**E**) Automated measurements of nodule area by Image J were performed on individual nodules (10 dpi) from *ann1-3* (n=494 nodules from 48 roots) and WT (n=556 nodules from 42 roots) from 4 independent experiments. (**F**) Nitrogen fixation capacity was measured in nodulated root segments of *ann1-3* (n=15) and WT (n=14) collected 21 dpi with *S. meliloti* from 3 independent experiments (and comprising respectively 365 and 417 nodules). Box plots in **D**-**F** represent the distribution of individual values (indicated as open circles in **D** and **F**, and as black dots in **E**). Median (central line), mean (solid black circle) and outliers (crosses) are indicated. WT boxplots are in grey, *ann1-3* mutant boxplots are in dark pink. Two-tailed t-tests (in **D** and **F**) or a two-tailed Mann-Whitney test (in **E**) of values were performed in R (asterisks indicate statistical differences; ****$p < 0.0001$; ***$p < 0.001$; **$p < 0.01$). (**G**-**N**) Detailed views of WT R108 and *ann1-3* mutant 15 dpi nodule sections. (**G**-**J**) In 1µm longitudinal sections stained with toluidine blue/basic fuchsin, meristematic (I), infection (II), interzone (IZ) and nitrogen fixing (III) zones are distinguished in WT nodules (**G**, **I**). The amyloplast-rich IZ and zone III are clearly defined in WT, while *ann1-3* nodules (**H**, **J**) show a much larger IZ like region, with starch over-accumulation and no zone III comparable to that observed in WT nodules. (**K**-**N**) Ultrastructural analyses by TEM of WT and *ann1-3* nodules. (**K**, **M**) Close up view of zone III of a WT nodule with uninvaded cells (UC) and invaded cells (IC) filled with bacteroids (asterisks in **M**). Arrowheads indicate amyloplasts located near intercellular spaces of IC. (**L**, **N**) *ann1-3* nodules also include IC with apparent differentiated bacteroids. However, they appear as bacteroids typical of interzone II-III (Vasse et al), imbedded in a region enriched in white vesicles (black asterisks in **N**). *ann1-3* nodules accumulate amyloplasts not only in IC (arrowheads), but also in UC. Scale bars: **A**-**C** = 1 mm, **G**-**J** = 50 µm, **K**-**N** = 5 µm.

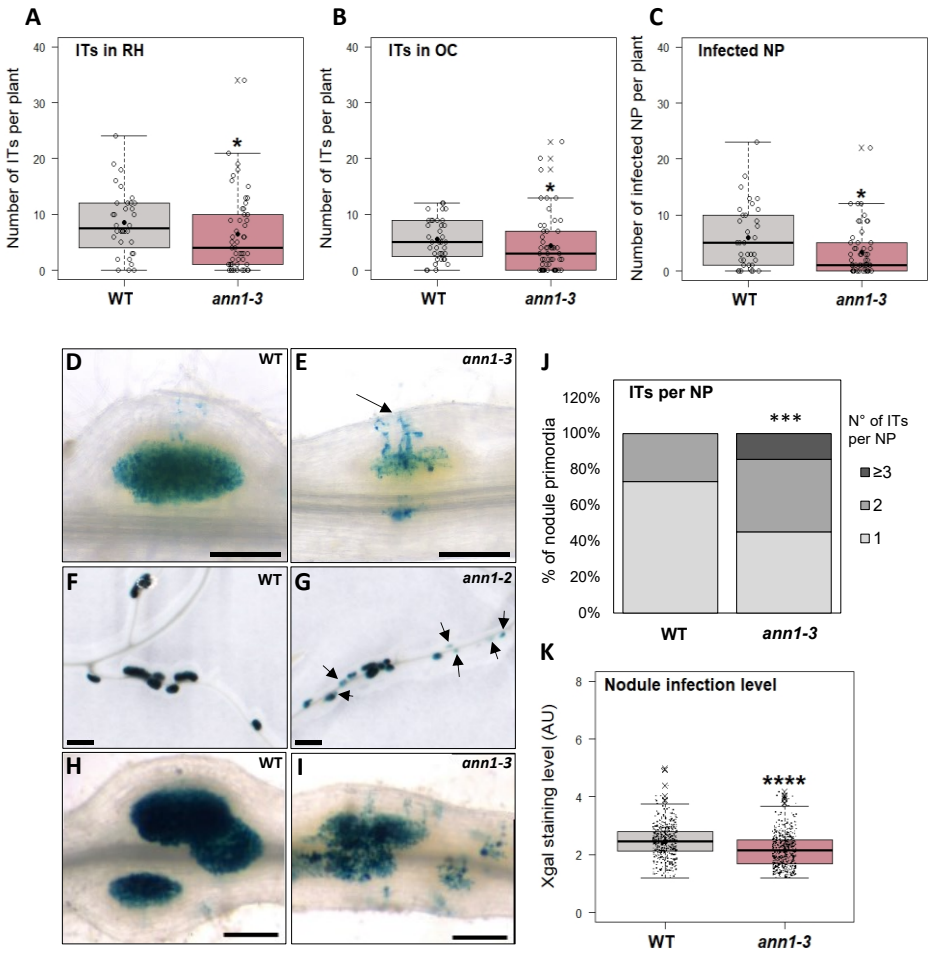

Fig. 6. Root Infection is negatively impacted in *ann1* mutants.

(**A**-**C**) Early root infection by rhizobia is less efficient in *ann1-3* than in WT at 4 dpi. Rhizobia infection was quantified in root systems of WT (n=36) and *ann1-3* (n=53) plants after histochemical X-gal staining to reveal infection events by *lacZ*-expressing *S. meliloti* rhizobia in blue. The number of root hairs with ITs (**A**), the number of infection sites with ITs that had reached the outer cortex (**B**) and the number of fully infected nodule primordia (**C**) were quantified from 3 independent experiments. Two-tailed Mann-Whitney tests of values in **A**-**C** were performed in R (asterisks indicate statistical differences, *p < 0.05; ***p < 0.001; ****p < 0.0001). (**D**-**I**) Representative images of WT and *ann1-2* or *ann1-3* infected nodules or emerging nodule primordia at 4 dpi (**D**-**E**) or 10 dpi (**F**-**I**). *ann1* mutant roots exhibit overall less colonized nodules (indicated by arrows in a global root view in **G**, and shown in close up views in **H** and **I**). (**J**) Frequency of nodule primordia at 4 dpi colonized by 1, 2 or 3 or more ITs. Colonization of *ann1* nodule primordia frequently occurs from 2 or more IT colonization sites compared with WT (arrowheads in **D**-**E**) (Chi square test, p=0.0005, ***). (**K**) Relative nodule infection level was quantified by automated ImageJ measurement of bacterial X-gal blue staining on 10 dpi nodules formed on WT (494 nodules from 48 plants) and *ann1-3* (556 nodules from 42 plants) roots. Box plots represent the distribution of individual values (indicated as open circles in **A-C**, and as black dots in **K**) from 4 independent experiments. A two-tailed Mann-Whitney test of values in R revealed significant differences (****p < 0.0001). Median (central line), mean (solid black circle) and outliers (cross) are indicated. WT is in grey, the *Mtann1-3* mutant is in dark pink. Scale bars: **D**-**E** = 250 µm, **F**-**G** = 1 mm, **H**-**I** = 1 mm.

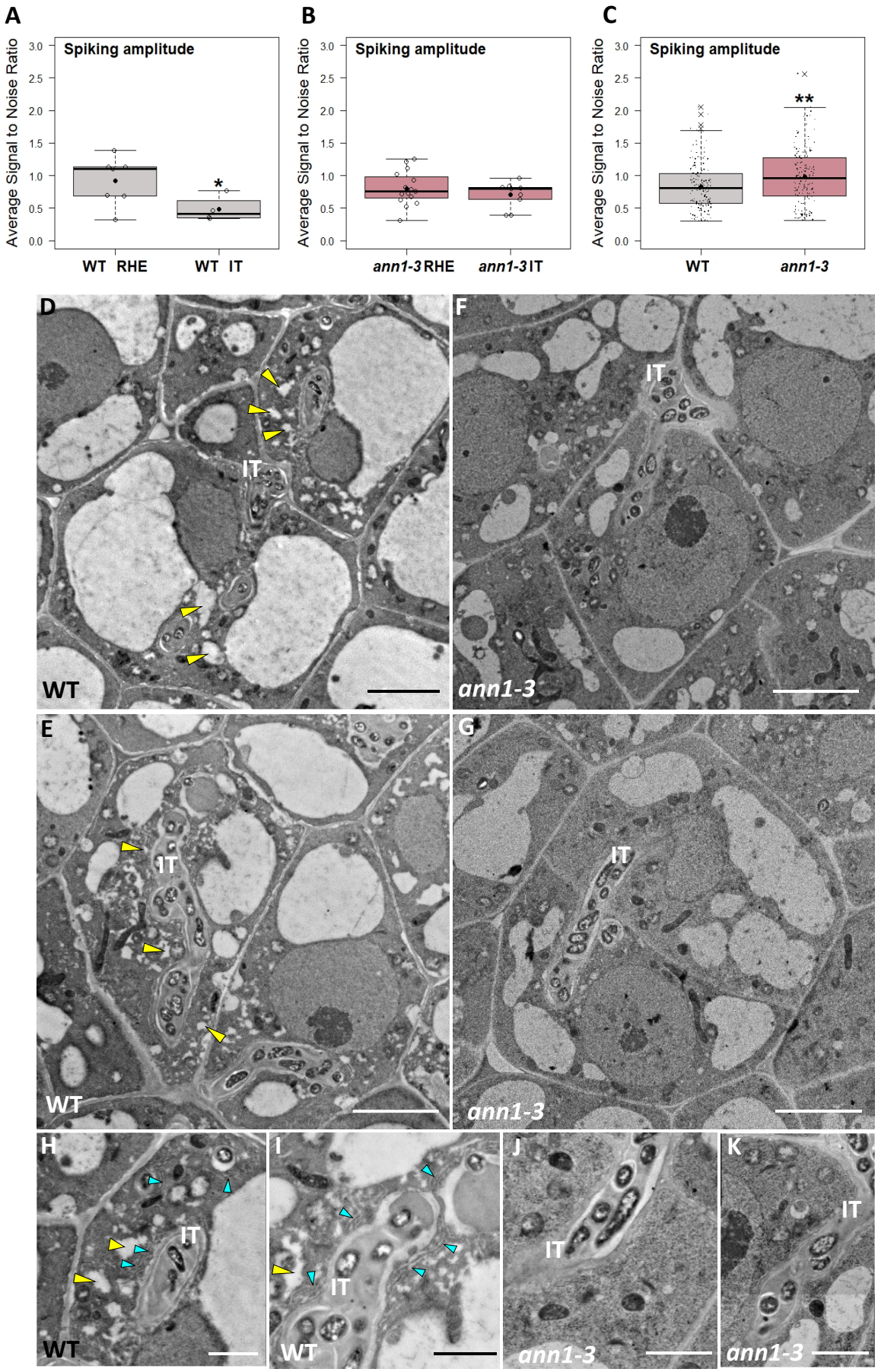
A
Spiking amplitude
Average Signal to Noise Ratio
3.0
2.5
2.0
1.5
1.0
0.5
0.0
*
WT RHE
WT IT
B
Spiking amplitude
Average Signal to Noise Ratio
ann1-3 RHE
ann1-3 IT
C
Spiking amplitude
Average Signal to Noise Ratio
**
WT
ann1-3
D
IT
WT
F
IT
ann1-3
E
IT
WT
G
IT
ann1-3
H
IT
WT
I
IT
WT
J
IT
ann1-3
K
IT
ann1-3

1263

1264 **Fig. 7. Modified Ca^{2+} spiking and IT cytoplasmic environment in the absence of MtAnn1.**

1265 (**A**-**C**) Transgenic roots expressing the NR-GECO1 Ca^{2+} sensor, were generated to monitor
1266 nuclear Ca^{2+} oscillations in genetic backgrounds mutated (*ann1-3*) or not (WT) in *MtAnn1*.
1267 Variations in Ca^{2+} ion concentration, through changes in the relative intensity of NR-GECO1
1268 fluorescence, is expressed as signal-to-noise ratio (SNR, cf. Methods section). Box plots
1269 represent average amplitude of spikes (spike SNR), calculated separately for each nucleus of
1270 root hairs with entrapped rhizobia (RHE) or with ITs in WT (WT RHE, n=7; WT root hairs with
1271 ITs, n=4) (**A**) or *ann1-3* (*ann1-3* RHE, n=15; *ann1-3* root hairs with ITs, n=9) (**B**) as well as *S.*
1272 *meliloti*-inoculated non-infected root hairs (**C**)(WT, n=160 and *ann1-3*, n=156) at 1-4 dpi. Data
1273 was obtained from three independent biological experiments. One-tailed t-tests (in **A**-**B**) and
1274 a bilateral Mann-Whitney test (in **C**) of values were performed in R (asterisks indicate
1275 significant differences, *$p < 0.05$; **$p>0.01$). Median (central line), mean (solid black circle)
1276 and outliers (cross) are indicated. WT is in grey, the *Mtann1-3* mutant is in dark pink. (**D**-**K**)
1277 Transmission electron microscopy analyses of infected cells from apical zone 2 of WT (**D**-**E**, **H**-
1278 **I**) or *ann1-3* (**F**-**G**, **J**-**K**) 15 dpi nodules. ITs in WT are embedded in vesicle-rich (yellow
1279 arrowheads) cytoplasmic bridges with visible ER network (blue arrowheads). These
1280 cytoplasmic features are not as prominently detected in *ann1-3*. Scale bars: **D**-**G** = 5 µm, **H**-**K** =
1281 2 µm.

1282

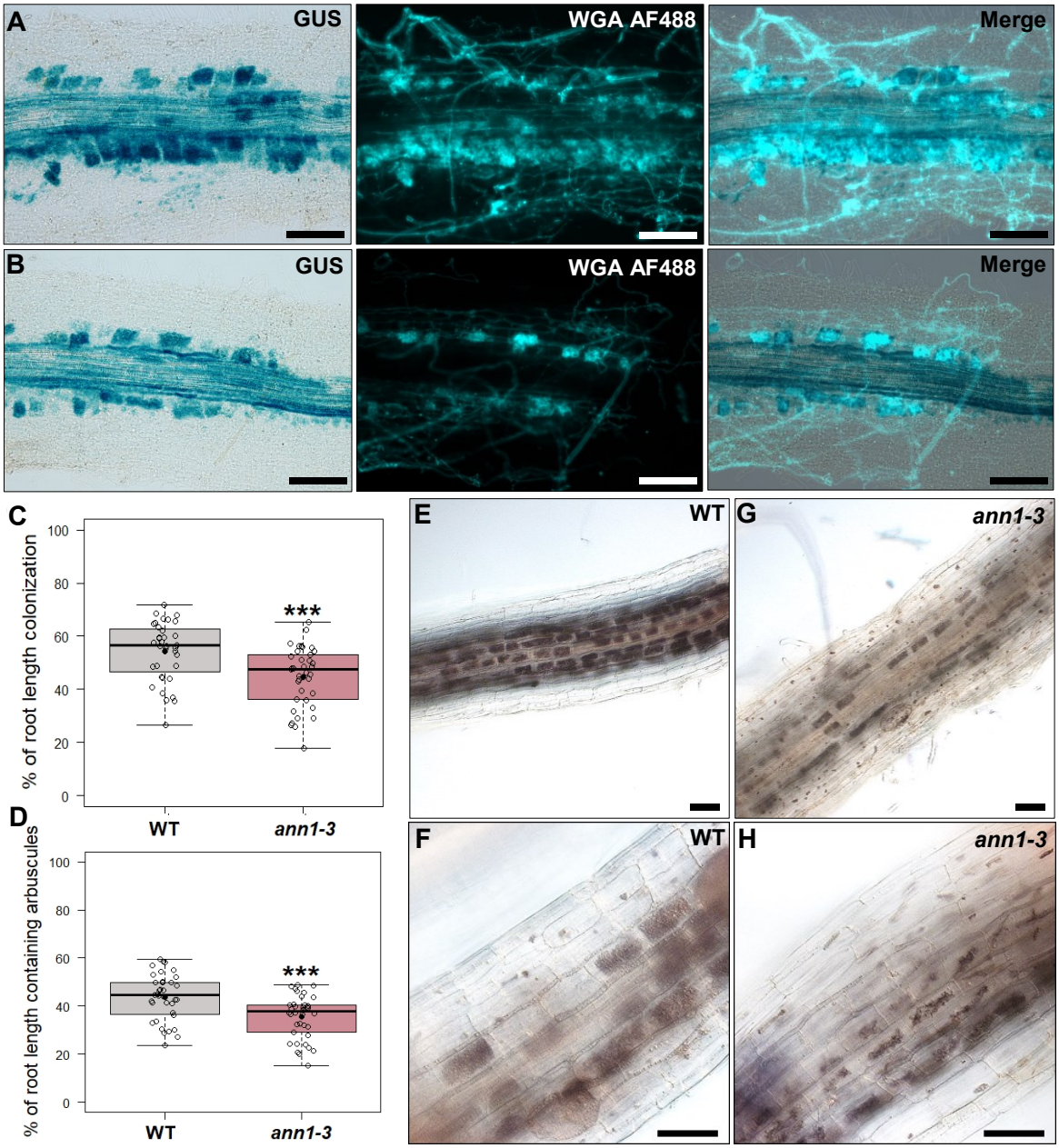

Fig. 8. *MtAnn1* is required for efficient mycorrhization *of M. truncatula* roots.

(**A-B**) *MtAnn1* promoter activity in independent *M. truncatula* roots colonized with *R. irregularis* at 4 wpi. Blue GUS staining correlates with *R. irregularis* colonized areas, visualized by WGA-AlexaFluor488 fluorescence staining. (**C-D**) Determination of intraradical colonization by *R. irregularis* in WT and *ann1-3* plants by the gridline intersect method. The relative surface of the root system displaying vesicles, arbuscules and/or intraradical hyphae is given in (**C**), while the relative surface corresponding specifically to arbuscules is given in (**D**). Box plots represent values from WT (n=36) and *ann1-3* (n=38) root systems at 6 weeks post-inoculation, from two independent biological experiments. Individual values (open circles), median (central line) and mean (solid black circle) are indicated. Two-tailed Student t-tests were performed. Asterisks indicate significant differences, ***p<0.001. (**E-H**) Representative pictures of ink

1295 stained AMF-colonized roots in WT (**E**-**F**) and *ann1-3* (**G**-**H**). Scale bars: **A**-**B** = 100 µm, **E**-**H**= 50
1296 µm.